Mohamed Nasralla Mahdy Nasralla

Distributed Acoustic Sensing (DAS) As a New Tool For Subsurface Imaging

June 2022

NTNU
Norwegian University of
Science and Technology

NTNU
Norwegian University of
Science and Technology

NTNU

Norwegian University of
Science and Technology

Distributed Acoustic Sensing (DAS) As a New Tool For Subsurface Imaging

Mohamed Nasralla Mahdy Nasralla

Norges Teknisk-Naturvitenskapelige Universitet
Department of Geoscience and Petroleum

NTNU

TPG4925- Petroleum Geosciences- Master's Thesis

Distributed Acoustic Sensing (DAS) As a New Tool For Subsurface Imaging

June 25, 2022

Mohamed Nasralla
Candidate No.10009

Supervisor: Prof. Børge Arntsen, IGP, NTNU

Contents

List of Figures

1   Abstract

Seismic imaging has been developed through last decades, that it becomes an important tool for subsurface imaging, which is used by various academic and exploration communities, helping them making better decisions when it comes to exploring for the natural resources inside the Earth. However, the traditional seismic acquisition techniques not only are too expensive, but also traditional sensors might not be suitable to be used in harsh environments, for instance, the sensor response might be affected by strong electromagnetic interference...etc. As a result, searching for new techniques for subsurface imaging that are cost effective and suitable to be used in harsh environments becomes so important. Distributed Acoustic Sensing (DAS) is a newly emerging technology that transforms submarine telecommunication cables into densely sampled seismic receivers that are cost effective and can make up for the limitations of the traditional sensors. DAS has been tested in this study to be used as an alternative method for subsurface imaging in the marine environment. The DAS data was a acquired in the Trondheimsfjord, Norway. A single channel streamer data has been acquired simultaneously, as a reference, to be compared with the DAS data. By checking the DAS directivity, we have found that DAS is more sensitive to longitudinal strains, that the maximum amplitude recorded by DAS is correspondent to a wavefield that impinges the cable with a horizontal incidence angle θ parallel to the direction of the cable orientation, the recorded amplitudes will decrease gradually as the incident angle θ increases, until the DAS cable becomes insensitive to the incoming wavefield at vertical incidence angle $\theta = 90^0$. Comparing the produced images, the one from DAS and the one from traditional streamer technique, both methods have a comparable signal two noise ratio, and both method were able to image the subsurface structure and the main reflectors, the seafloor and basement top, were imaged successfully. DAS has a lower resolution compared to the streamer data, however, using wide azimuth acqusition and an energetic source will be effective to make up for the amplitude loss due to the DAS directivity, moreover, decreasing the gauge length will be helpful to increase the spatial resolution and lower frequency enhances wave penetration inside the Earth.

2 Introduction

Subsurface imaging is extremely important, not only for the academic purposes that mainly focus on imaging of the interior structure of the Earth to understand the nature of different forces inside the Earth, for instance, the forces that derive plate tectonics, but also, having a correct image that is more representative of the subsurface helps to make correct decisions when it comes to exploring for Hydrocarbons and deep water mining.

2.1 Sismic Exploration

Traditional seismic exploration methods provide an accurate and confident way for both shallow and deep subsurface imaging through sophisticated seismic data acquisition and processing techniques, developed through last decades. Thus, that makes it possible to map even tiny structures and small ruptures in the subsurface ([14] Monrigal O., Duarte H., 2017). Seismic survey designs can be manipulated to fit the main purpose of a specific study. For example, for marine oil and gas exploration, large vessels that are capable of towing long hydrophone streamers reach to several kilometres can be used. However, in areas characterized by complex geological setting, this conventional towed-streamer seismic survey is not the most convenient way to get the proper image of the subsurface ([1] Thompson M., Arntsen B.,and Amundsen, L., 2007). Using Ocean bottom cable (OBC), at which the cables are laid on the ocean floor, where they record seismic data, has demonstrated its advantages over the floating streamer technique, see (Figure 1).
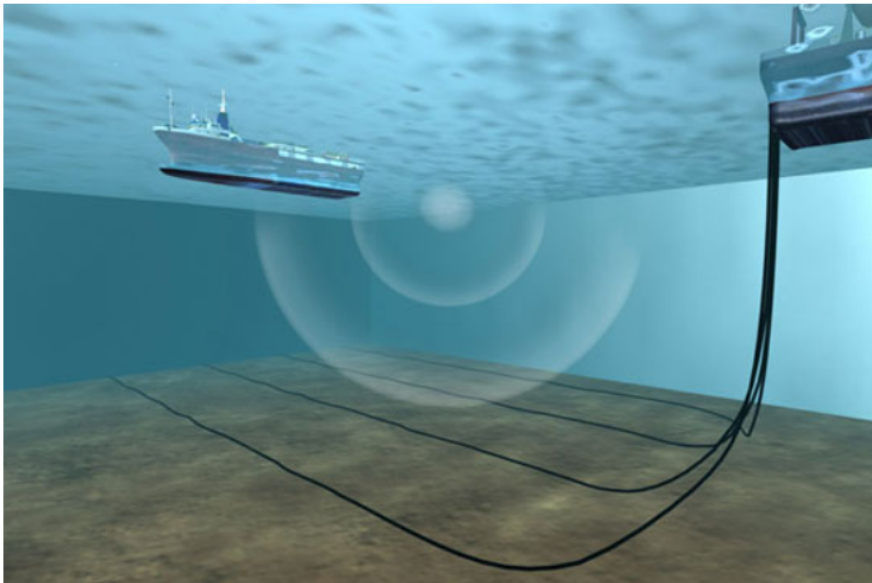
Figure 1: Image of a source vessel sending out P-waves to the ocean bottom cables (Credit source :Peak Seismic Solutions [16])

Ocean Bottom Seismometer (OBS) system can be used for the academic research purposes as well, to get information about the deeper parts of the Earth's crust and the upper mantle . OBS are devices consist of a hydrophone and 3C seismometer to record long offset seismic or seismological data. The OBS system can be relocated on the sea floor, and has the ability to function down to 6000 m water depths. In order to cover a lager area, several OBS devices can be deployed several kilometers apart ([15] Dondurur D., 2018).

According to ([2] Landrø, M., and Amundsen L., 2018) seabed seismic acquisition is more superior over towed-streamer techniques, not only because compressional and shear waves can be recorded, which ends up with high quality, high fidelity and less noisy image of the subsurface, but also helps to illuminate the structure from different angles through providing a wide range of offsets and angles that can be used between source and receivers, see (Figure 2), however, it requires tremendous technical preparations to acquire seismic surveys using these techniques, moreover, it's too expensive when accounting for the high cost equipment used and the number of personnel required to successfully conduct an accurate survey. In addition, permissions are mostly required before conducting any seismic survey too.

(a) 3D marine streamer   *(b) 3D OBS*
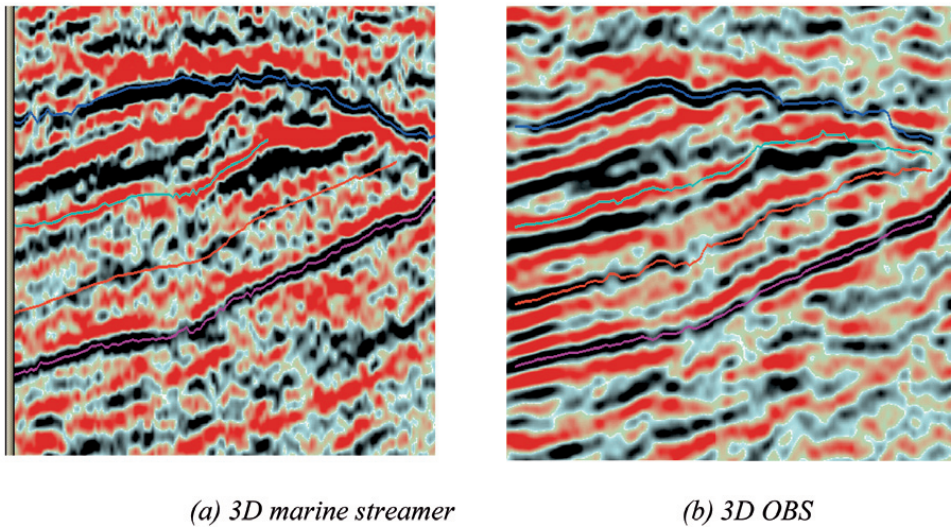
Figure 2: 3D OBS image of the Statfjord field showed improved definition relative to the conventional 3D marine seismic image(credit:[1]).

Near-surface seismic imaging can be used for characterization, monitoring and assessment of any potential geological hazards like near surface faults, soil stability, or leakage of shallow gas. All of which have their impacts, that might be devastating for offshore activities like wind farm and drilling platforms ([3] Taweesintananon K. and Landrø M., 2021). " A high temporal-spatial resolution, low maintenance cost, and less intrusion to nearby life are required for urban subsurface monitoring" ([4] Fang G., 2020).

Electroacoustic sensors, are sensitive to acoustic waves. However, in addition to their cost, they are not suitable to function in all environments. Most of these elctroacoustic sensors can be easily affected by strong electromagnetic interference, flammability...etc, ([36] Wang, Y., Yuan, H., 2019). As a result, searching for new alternatives becomes more important to make up for the limitations of the traditional electroacoustic sensors.

2.2   Distributed Acoustic Sensing (DAS)

Distributed Acoustic Sensing (DAS) is a newly emerging technology that transforms submarine telecommunication cables into densely sampled seismic receivers that are cost effective ([9] Dou S. and Lindsey N., 2017). DAS can be used for static temperature and strain measurement ([38] Dong Y. and Zhang H., 2012), and it combines interference sensing technology, optical backscattering technology, optical coupling detection technology and optical nonlinear parameter detection technology ([39] Weng Y. and Wang T., 2016), see (Figure 3).
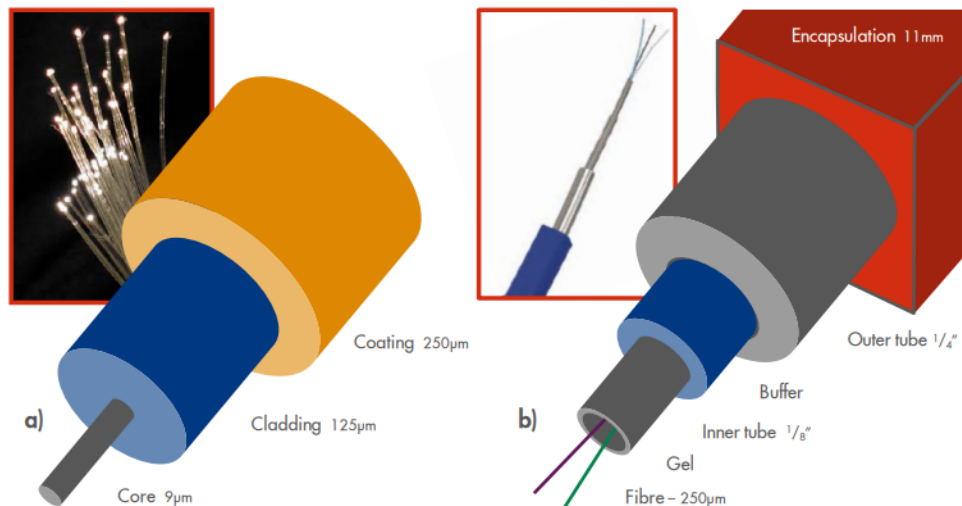
Figure 3: simplified sketch of the build-up of a typical optical fibre (a) DAS cable usually is made up of several layers: due to the refractive index contrast between the core and the cladding, laser light typically is transmitted through the core, a coating is added to enhance the cable strength (b) For down-hole applications, fibres are typically packaged in a metal control line, and a plastic buffer separates between the inner and outer metal tubes (Credit:[6] Lumens P. G. E. , 2014)

DAS has been successfully examined as an alternative recording system for down-hole seismic ([5] Parker et al., 2014). Various applications of DAS in oil and gas wells have been studied by ([6] Lumens P. G. E. , 2014). Moreover, other studies have been conducted to examine other various application for (DAS), for instance, ([7] Lindsey, N. J. and Biondi B. , 2020) used DAS for urben traffic monitoring during the COVID-19 pandemic. ([17] Kowarik S and Schubert M., 2020) used DAS for monitoring extended railway infrastructures for precise tracking of train position, speed, and the number of train cars. ([8] Ajo-Franklin, J. and Lindsey, N, 2015) used DAS data for ambient noise analysis. ([18] Ajo-Franklin J. and Dou S., 2017) Monitored permafrost thawing using DAS data.

DAS shares the same principle as other electroacoustic sensors and it uses original optical fiber as a sensing element, that allows the measurement of thousands of points at the same time, in addition, the measured physical parameter has its own particularity, that allows DAS to be used in some harsh environments, where the traditional electroacoustic sensors can't function with reliability ([36] Wang, Y.and Yuan, H 2019). According to ([37] Ma, G. M. and Zhou, H. Y., 2018) DAS has its own advantages over the traditional acoustic sensors, such as anti-electromagnetic interference, low long-distance transmission loss, good concealment and corrosion resistance. In addition, based on the interferometric sensing principle of optical sensors, dynamic measurements can be acquired effectively with ultra-high resolution and high dynamic range ([40] Langhammer J., Eriksrud M. and Nakstad H, 2010).

In contrast to ocean-bottom cable's (OBC's) acquisition system which consists of immense electronic networks, or to ocean-bottom nodes (OBN) which powered by internal batteries, which requires an effective power management plan, no electronic or electrical power devices are required at the sensing points with fiber-optic cables ([3] Taweesintananon K. and Landrø M., 2021), which is an advantage that gives rise to a more reliable sensing system, as the cable itself works as the sensing element, without any additional transducer.

A DAS system functions in a way that it makes use of a single optoelectronic interrogator unit (Figure 4), which has the capability of sampling a long optical fiber cable up to several kilometers at sub-meter channel spacing ([9] Dou, S., Lindsey, N., 2017). DAS measures the dynamic strain using the phase interferometry principle ([12] Hartog, 2017). The DAS instrument, the interrogator, sends short laser pulses into the optical fiber, the backscattered signal from multiple pulses when the fibre is at rest is constant. However, a deformed cable causes the travel time to sections of the fibre beyond the point of deformation changes, as a result, the the backscattered signal will be changed, see (Figure 5). The interrogator measures the subtle phase shifts of Rayleigh scattered light returning to the detector at a predicted two-way travel time ([11] Posey, 2000)
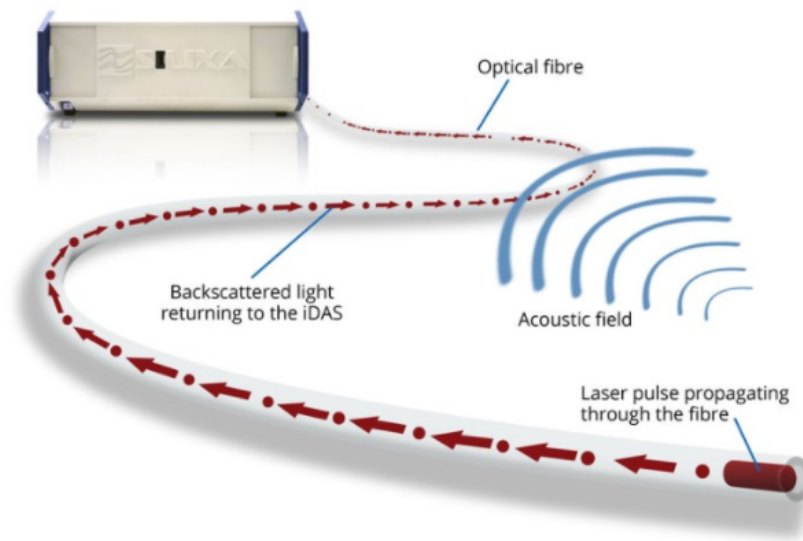
Figure 4: A typical DAS recording system, an interrogator is used to send laser pulses through the cable and they continuously reflected to the interrogator due to the Rayleigh backscattering process inherent to all optical fibers, Credit : Silixa [20]
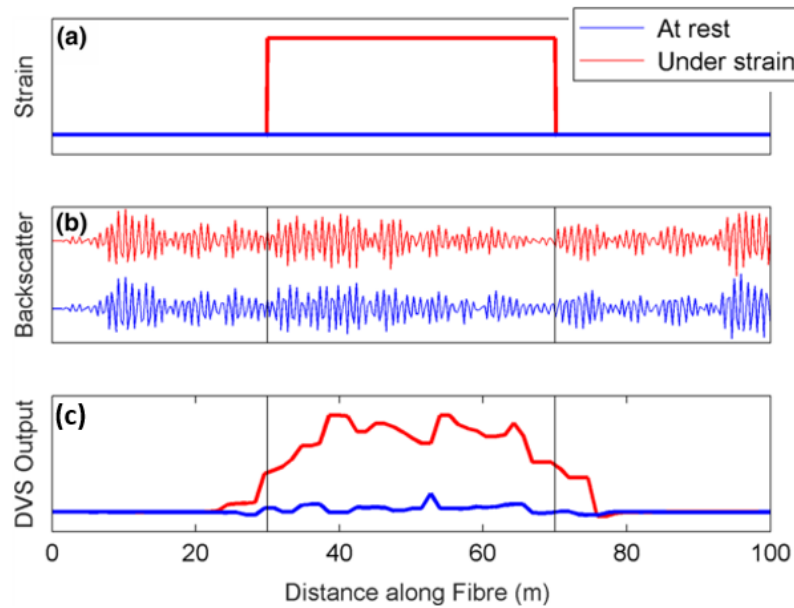
Figure 5: Two synthetic (a) strain, (b) backscatter, and (c) Notice the difference in the DVS output profiles for the fibre at rest (blue lines) and undergoing localized strain (red lines). The profiles were generated, assuming the acquisition method of Hartog and Kader (2012), Credit : [41]

As the phase of the reflected optical light is proportional to the strain of the fiber, time - to - distance conversion allows strain signals to be recorded at spatially localized regions of the fiber, hence, transforming the cable into a densely sampled sensor array ([7] Lindsey, N. J. and Biondi B., 2020). The gauge length, which is the distance over which the phase-shift is estimated at each receiver, is mostly fixed for each experiment ([43] Bakku, S. K. and Wills, P., 2014). Average strain recorded by DAS channel can be related to the point strain using the following equation:

$$R = \frac{sin(\frac{K_x G}{2})}{\frac{K_x G}{2}} \frac{sin(\frac{K_x L}{2})}{\frac{K_x L}{2}} \tag{1}$$

where G and L are gauge length and pulse width respectively, whereas k_x is wavenumber projection along the cable, see (Figure 6).
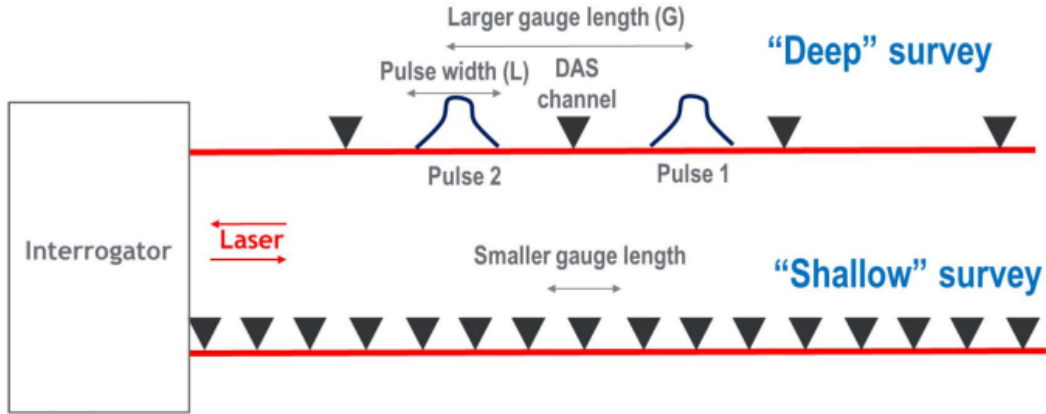
Figure 6: Schematic of measuring dynamic strain using two reference pulses of light propagating along an optical DAS fiber, notice the difference between the two acquisition schemes for both Deep and Shallow surveys : credit[19].

2.3 Objective of the study

DAS application in the marine environment has not been intensively presented. There are two main objectives of this study. First, checking the DAS directivity, which is the sensitivity of DAS to the direction of the incoming wavefield. A second objective is to investigate the possibility of using DAS as an alternative technique for subsurface imaging in the marine environment using SHEARWATER REVEAL as the main processing software, to process DAS data that has been acquired in the Trondheimsfjord, Norway. Then, compare the results obtained from DAS to results obtained from traditional marine streamer data that has been acquired simultaneously with the DAS data after processing the data from both methods.

3   Geological background of the study area

3.1   Geological setting

A series of east to southeasterly transported nappes composed The Caledonide orogen in central Norway, at which they were affected by a series of regional scale folds, extensional faults and large detachments, that was followed by transection by a major, multiphase strike slip fault system of the Møre-Trøndelag Fault Complex (MTFC) ([27] Roberts D., 1998).

Figure 7: Relief map outlining the present drainage area towards Trondheimsfjord (ca. 20 000 km^2). The ice margin in early Younger Dryas is shown with a dotted line (Tautra Moraines). A=Agdenes, E=Edøyfjorden, T=Tjeldbergodden, H=Hegra, S=Straumen. Figure credit[29].

Based on isotopic , fission-track and paleomagnetic studies , the fault complex has passed through a number of principle stages of movement ([30] Bøe R. and Bjerkli k., 1989, [31] Grønlie A. and Torsvik T., 1989). These include ductile sinistral offset in Early/Mid Devonian time, and ductile - to - brittle dip slip and mainly dextral strike- slip/oblique-slip displacement in Late Devonian, Permian-Triassic, Late Jurassic/Early Cretaceous and Late Cretaceous/Early Teriary time ([27] Roberts D., 1998).
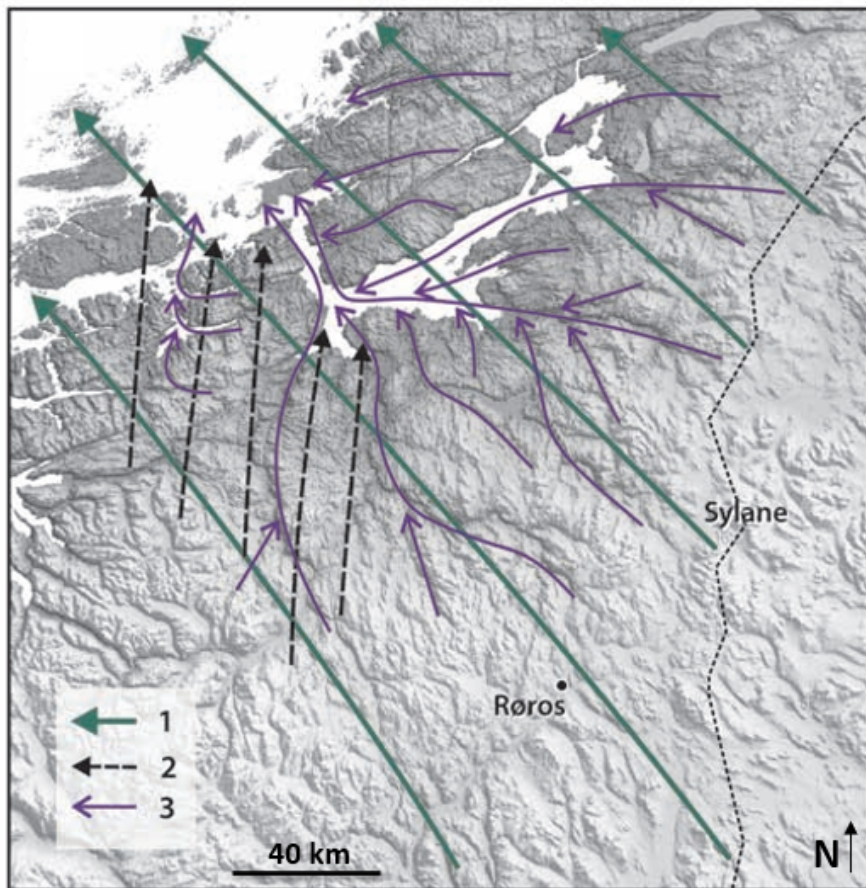
Figure 8: Directions of ice movement, Notice how the topography controlled the ice movement direction : 1 = oldest (LGM); 2 = intermediate; 3 = youngest. Figure credit: [29]

The Trondheim Nappe Complex covers a large part of the central Norwegian Caledonides and constitutes the upper allochthonous nappe complex within the Caledonian tectonostratigraphy ([34] Roberts and Wolff, 1981). According to ([42] Wolff, 1976) the Precambrian–Silurian westward dipping metamorphic and volcanic rocks, schist and tuff in particular, formed most of the bedrock around Trondheim.

Trondheimsleia exists a long the trace of the Hitra-Snåsa Fault of the Møre-Trøndelag Fault Complex (MTFC) ([28] Bøe et al, 2005), However, the Trondheimsfjord has been affected by another major fault of the MTFC from Orkdal to Verdal, at which it forms a deep fjord system with several main branches in the extension of the valleys Orkdalen, Gauldalen, Stjørdalen and Verdalen. However, The deepest basin (500-617 m b.s.l.) is located between Trondheim and Agdenes ([29] Rise L., Bøe R., 2006).

The ice movement followed a predefined directions, at which they were controlled by the topography as the ice thinned and the ice margin receded ([32] Reite A., 1994), see (Figure 8). According to ([33] Svjeian H., 1997) the time interval between 12.5-9.5 ka C^{14} BP was a period, at which the ice recessional lines for the Trondheimsfjorden area can be delineated.

3.2   Stratigraphy

According to [35] L'Heureux who studied the stratigraphy of the area using seismic data, facies analysis of gravity cores and C^{14} AMS dating, The stratigraphy can be divided into three main units as follows:

3.2.1   Unit One

Unit one represents the basement rock, which is often found at different depths and is characterized by a seismic facies of chaotic to hyperbolic reflections with a distinct top boundary due to the huge difference in acoustic impedance between the basement and the overlying sedimentary rock.

3.2.2   Unit Two

Unit two comprises deposits of Allerød and Younger Dryas (Al/ YD) age, which is glacio-marine sediments with drop stones from sea ice and/or iceberg that overlie bedrock, to form a thick succession of deposits of range 18–50 m thick. It has a seismic facies that is characterised by continuous and low to medium amplitude stratified seismic reflections directly on top of the bed rock.

3.2.3   Unit Three

Unit three overlies unit two and consists of Holocene deposits of bioturbated clay, silty, and sandy sediments, overlain by poorly sorted sand. This unit can be subdivided into three sub-units as Early Holocene, Mid- Late Holocene and Late-Holocene to Recent. it is characterised by high amplitude seismic reflections with more transparent acoustic intervals.

4 Data

The DAS Data has been acquired during a marine seismic survey in the Trondheimsfjord, Norway. A research group from NTNU has acquired this survey , using NTNU's research vessel, the R/V Gunnerus. In this survey, a single marine seismic source and a single-channel hydrophone streamer are towed behind the vessel. The HMS-620 Bubble-Gun recording system, which is a simple recording system consisting of an HMS-620 Bubble Pulser, an electric seismic source, and a short hydrophone streamer with 7 m of a single-channel array comprising 24 elements, with subbottom sonar interface software from National Instruments, has been used to record seismic data from the streamer. The acquisition geometry can be simply represented by (Figure 9).
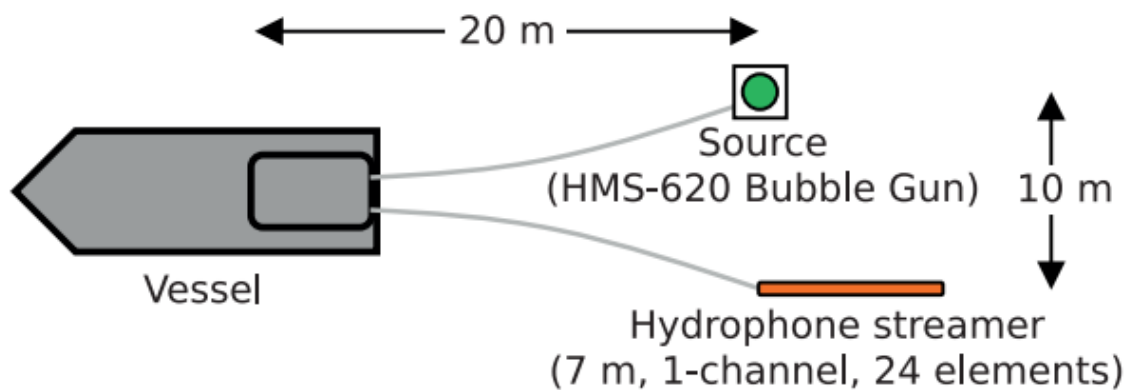
Figure 9: A Schematic representation of a top view of the acquisition lay out, the source and streamer are towed approximately 20 m behind the vessel, at which they are at depth around 1 m below see surface and separated by a 10 m distance from each other, Figure Credit: [3]

The source and streamer depths are approximately 1 m below the sea surface, they are towed approximately 20 m behind the vessel's reference position, and separated by 10 m perpendicular to the sail line. The recording start time is synchronized with the gun firing time. The recording time sampling interval is 0.25 ms, and the maximum recording time for each shot is 266.25 ms. The source energy is approximately 50 J, which is equivalent to 200 dB relative to the reference pressure 1 µPa at reference distance 1 m. The frequency bandwidth ranges from 350 to 1000 Hz at 10 dB down, the dominant frequency is approximately 600 Hz. The shot time interval, which is the gun firing time interval, is set to 267.75 ms in the system . Simultaneously, seismic data was recorded using an OptoDAS interrogator connected to a dark fiber in a seafloor telecommunication cable. The DAS recording system is independent of the vessel's equipment, where the

vessel is navigated as close to the DAS cable as possible. The vessel average speed is 2 knots to acquire high-density seismic data with minimal noise from the vessel's propulsion. Hence, the average shotpoint interval is approximately 0.275 m. The map of the source line and DAS cable is shown in Figure (10).
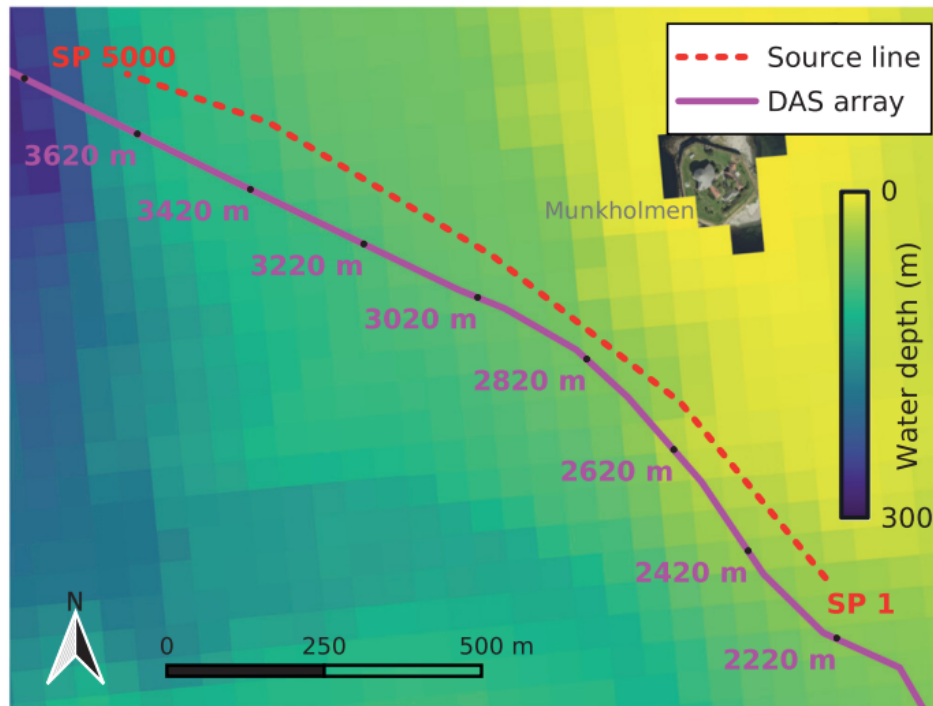
Figure 10: Survey map of the marine seismic survey in the Trondheimsfjord, Norway. The dashed red line represents the vessel route, and the solid magenta line represents the DAS receiver cable. The background water depth map is shown, courtesy of the Kartverket (Norwegian Mapping Authority) Credit: [3].

Using the already existing telecommunication cable in the Trondheimsfjord, The Opto-DAS interrogator is connected to one end of this cable, at which the cable laid into the soft sediments at approximately 0–2 m below the seafloor of the fjord from Trondheim to Kvithylla. A single-mode silica fiber, SMF-28, in the cable is used in this experiment. A time-sampling interval of 0.44 ms was used to continuously record The DAS data, The channel spacing is 2.04 m, whereas the gauge length is 4.08 m.

While the streamer data has been acquired using a single channel, DAS data was continuously recorded along the cable with many more recording channels. An accurate gun firing time of the source should be known and used to extract a shot profile from the continuously recorded data, to rearrange the continuously recorded DAS data into several shot profiles. Due to the acquisition limitation of not having a synchronous sampling of the DAS and streamer recording systems, the Coordinated Universal Time (UTC) time stamps of the gun firing from the recorded streamer data was used to extract different shot profile.

Another data acquisition limitation is that the streamer data are recorded in SEG-Y format, at which time stamps of an accuracy of 1 s are stored in this format, conversely, DAS data are recorded using 0.44 ms recording time interval, As a result, it is tricky to define the exact time sample in the DAS data when the gun is fired from the given time stamp with lower precision. A data-driven method has been proposed by ([3] Taweesintananon K. and Landrø M., 2021) to estimate the start time of each shot record from the corresponding first-arrival time in the DAS data to get across this challenge. By Assuming that the DAS receivers are on the seafloor, the first arrival event at near offsets is the direct wave propagating from the source to DAS receivers as shown in (Figure 11), more details about this method is introduced in the method section .
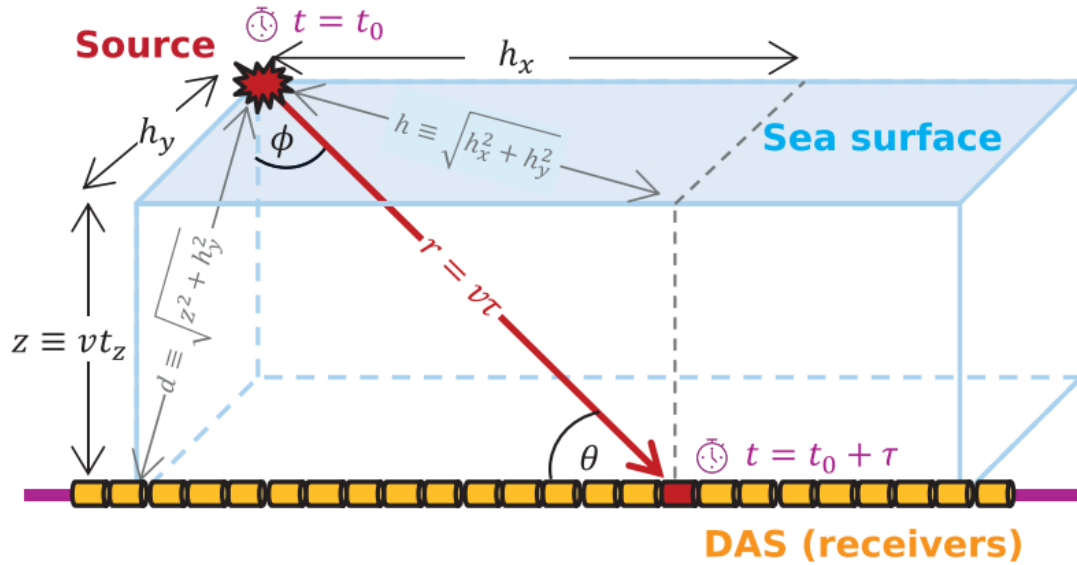
Figure 11: A schematic representation to illustrate the method used to determine separate shot profiles, this method used to estimate the shot position as well, where τ , is the traveltime of direct wave propagation with velocity v from the source to a receiver at the inline offset h_x. Figure credit: [3].

The source-to-cable distance (d) can be estimated by using time picks of the first arrival at the inline offset of $h_x = 0$ and any h_x. Then, the start UTC time of a DAS shot

record (t_0) using the following expressions :

$$d = \frac{v}{2\Delta\tau} \left(\frac{h_x^2}{v^2} - (\Delta\tau)^2 \right) \tag{2}$$

and

$$t_0 = t_{\{h_x=0\}} - \tau_{\{h_x=0\}} = t_{\{h_x=0\}} - \frac{d}{v} \tag{3}$$

where v is the P- wave velocity in the sea water, t is the picked UTC time at which the direct wave arrives at a receiver on the DAS cable. τ is the traveltime for the wave that propagates directly from the source to a receiver, and $\Delta\tau = \tau_{\{h_x\}} - \tau_{\{h_x=0\}}$, where $\tau_{\{h_x=0\}} = \frac{d}{v}$. Assuming velocity in water 1500 m/s, by using this expressions, we can derive the start UTC time of every shot and construct individual shot profiles of DAS. Equation 2 can determine the distance (d) between the source and DAS cable, even if no information of the source position is given, Consequently, equation 3 requires no source parameter to determine the gun firing time. Using this method, it was found that the actual gun firing time interval is slightly shorter than the value that was set to the shooting box. Moreover, given the water depth (z) of a receiver, we can estimate the crossline offset (h_y) using the expression:

$$h_y = \sqrt{d^2 - z^2} \tag{4}$$

The estimated shot positions relative to the DAS cable can be seen in (Figure 12).
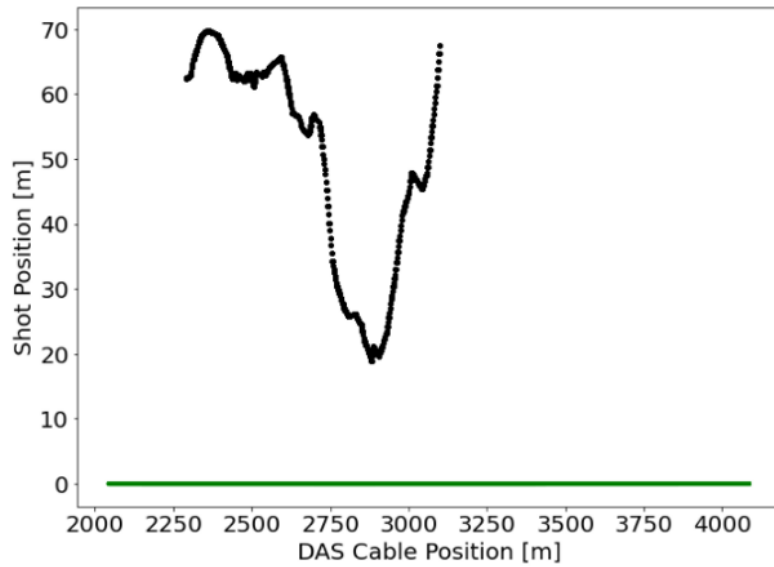
Figure 12: A Figure to show the relative shot positions relative to the DAS cable. The green straight line represents the DAS cable and the black dots represent different shots.

In order to apply this method, the DAS cable was assumed to be straight, that might introduce some error when trying to set the geometry, fortunately, the introduced error was small enough to have a significant implications of the final results. Short offset receivers usually reflect stronger reflections of the subsurface structures, Unfortunately, this data set lacks zero offset data.

4.1   Raw DAS Data

Three thousand shots of the DAS data were selected. As it can be easily seen from (Figures 13-16) that show some examples of the raw DAS data that the data has been masked by high frequency noises. A simple band pass filter will be effective to discard these kind of noises. The hyperbolic shape in (Figure 14) represents the direct waves that travelled directly from the seismic source to the DAS cable. Only around 80 shots in the raw data that show these kind of direct arrivals. No clear subsurface reflections have been observed in the raw DAS data. It is interesting that the seafloor geometry can be figured out directly by using the direct arrivals, as the DAS cable exists on the seafloor at 0-2 m approximate depth.
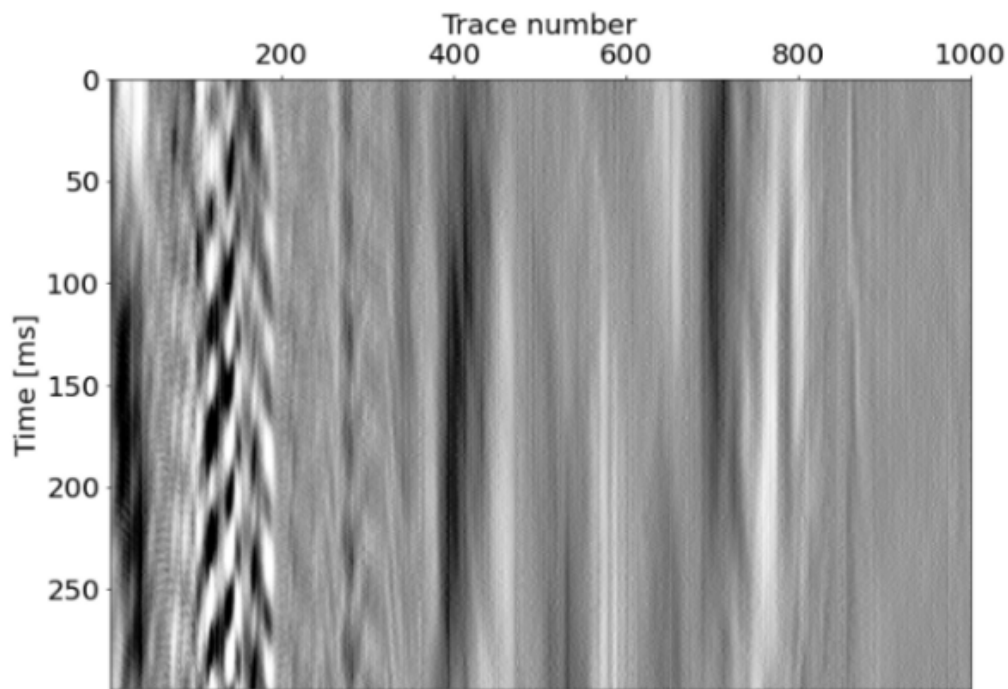
Figure 13: Shot number 36 of the raw DAS data.
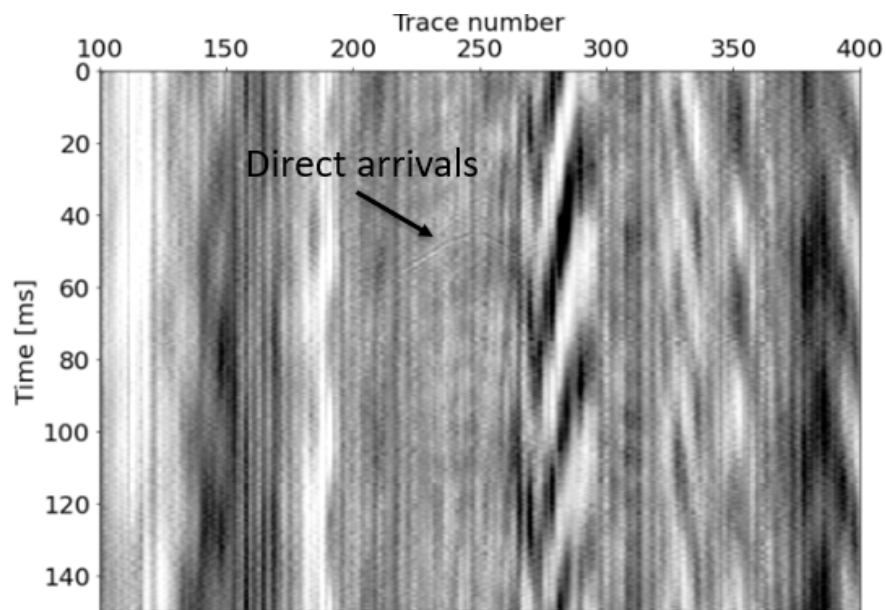
Figure 14: Shot number 940 of the raw DAS data, Notice the hyperbolic shape that represents the direct arrivals of waves that travelled directly from the seismic source to the DAS cable.
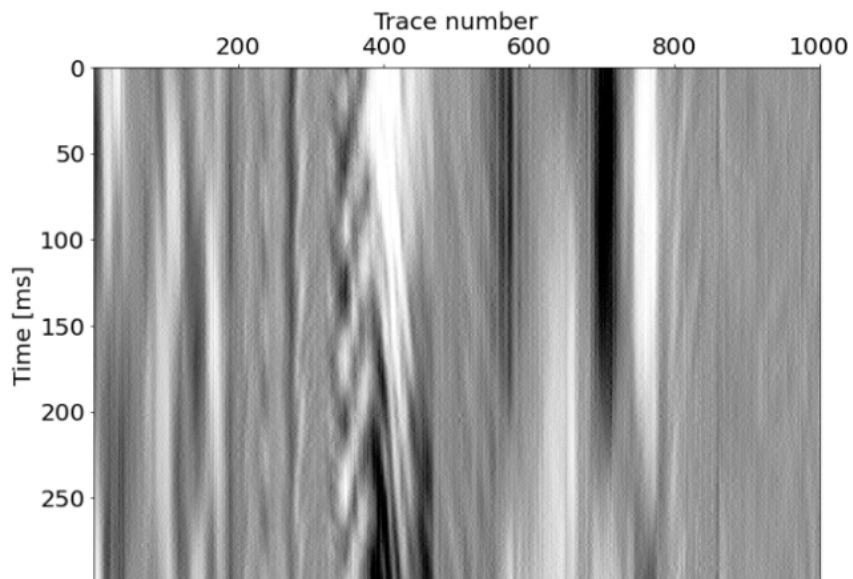
Figure 15: Shot number 1730 of the raw DAS data
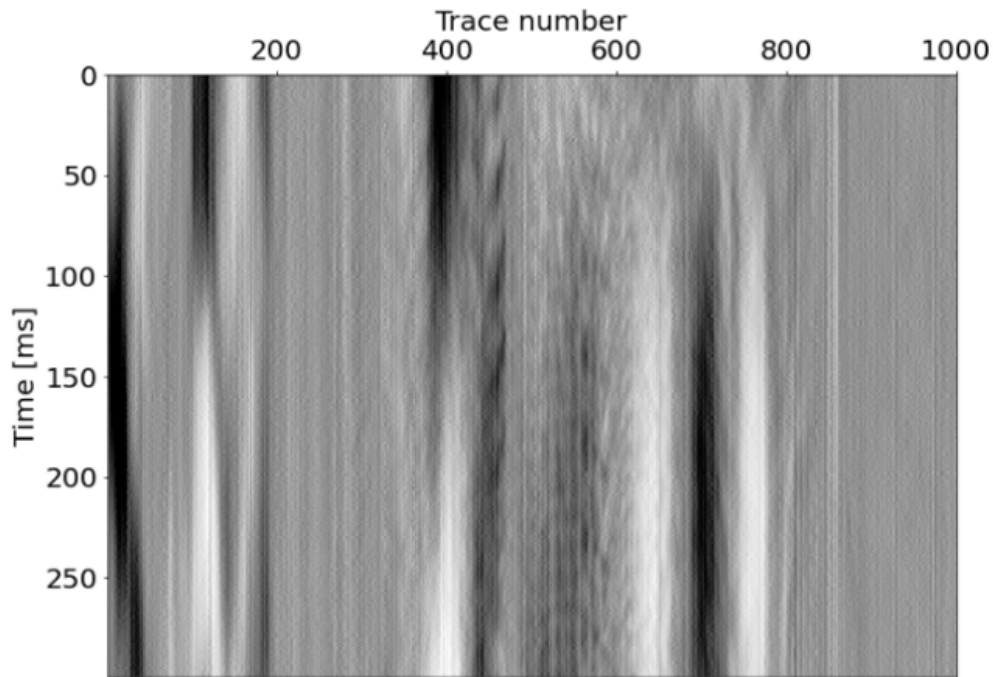
Figure 16: Shot number 2900 of the raw DAS data

4.2   Raw Streamer Data

Comparing the output from the data acquired from DAS with the output obtained from traditional marine seismic acquisition by the streamer will be helpful to evaluate the quality of the DAS data. The raw streamer data can be seen in (Figure 17), it is easily to diffrentiate between three main events in the figure. The first event, marked by (A), is the direct arrivals travelled directly from the source to the streamer, it is considered here as a kind of noise and it will be eliminated later on the processing sequence of the streamer data, the second event, marked by (b), represents the seefloar reflections. However, the third event, marked by (c) is the top of the bedrock, reflections below this event have a Chaotic nature with no clear geometry.
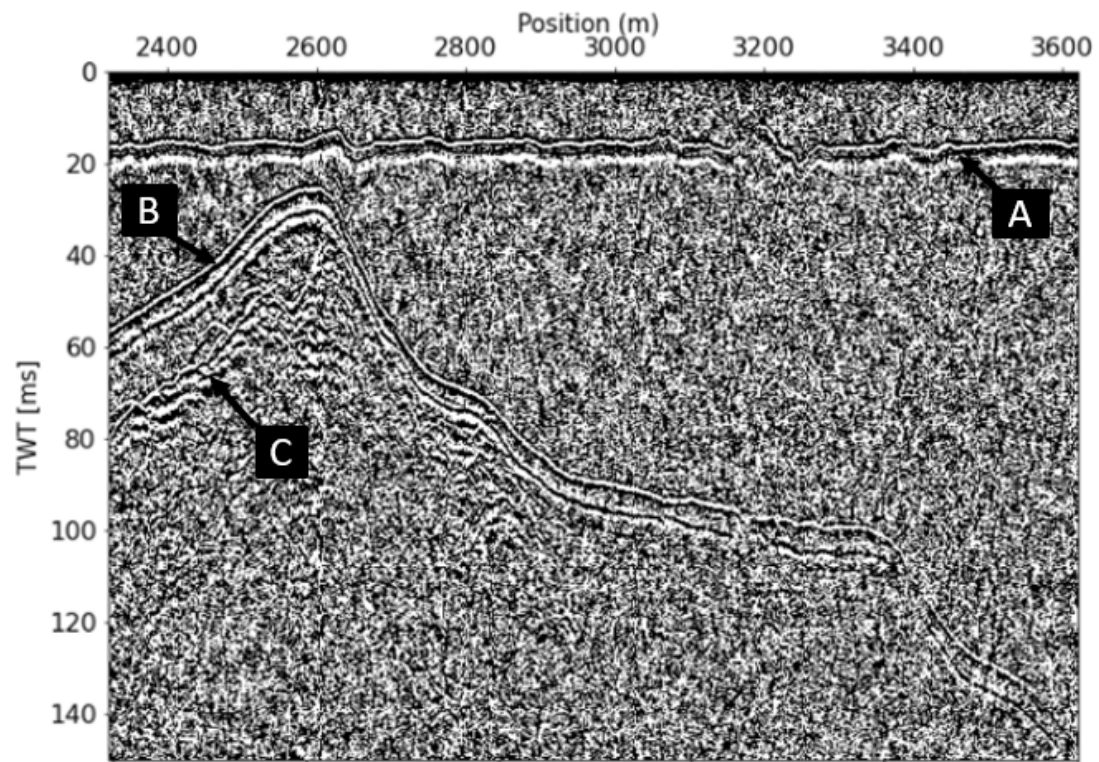
Figure 17: Streamer Raw Data from a common channel gather. Notice the three events marked by (A) which is the direct arrivals, (b) represents reflections from the seafloar and (C) is the top of the bedrock.

5   Methods

The methods section is subdivided into five subsections, where we will introduce the theory behind the DAS technique and we will summarize the the processing sequences we used to process both the DAS data and the streamer data. More details about the DAS technique theory can be found in ([3] Taweesintananon K. and Landrø M., 2021).

5.1   DAS recording system

Pulses of light with a free space wavelength λ_0 of 1550 nm have been continuously sent through the DAS cable. The Spatial sampling interval (SSI) can be defined as:

$$SSI = \left(\frac{c}{2n_g}\right)\Delta\tau \tag{5}$$

where $c \approx 3*10^8$ m/s is the speed of light in vacuum and $\Delta\tau$ is the sampling period at the optical receiver which in our case approximately is equal to $1*10^{-8}$ m/s and $n_g \approx 1.47$ is the refractive group index of the SMF-28 fiber used in our experiment. applying (Equation 5), we get $SSI \approx 1.02$ m. In this experiment, a cable length of 44 km was used, at which the maximum number of recording channel is 44000, this can be determined through the value of $\Delta t/\Delta\tau$.

Now, consider a spacial sampling location x, at which the the phase of the backscattered light ϕ_x can be expressed in radians as:

$$\phi_x = \frac{4\pi n_g x}{\lambda_0} \tag{6}$$

The time-differentiated phase ($\dot{\phi_x}$) which is the rate of phase change between consecutive time samples associated with this location (x) can be extracted and defined by the interrogator. A spatial moving average has been applied to the time-differentiated phase ($\dot{\phi}_{avg,x}$) around the location x to adjust the SSI to the desired spacial resolution. The resolution in this experiment was calculated by averaging across four spacial samples ($N_{avg} = 4$) to achieve a full width $L_w = N_{avg}*SSI \approx 4.08$ m. The time-differentiated phase change ($\Delta\dot{\phi_x}$), which is the difference of the average time-differentiated phases between the two spatial locations separated by four spatial samples, can be easily calculated through:

$$\Delta\dot{\phi_x} = \Delta\dot{\phi}_{avg,x+L_G/2} - \Delta\dot{\phi}_{avg,x-L_G/2} \tag{7}$$

where $L_G = N_{\Delta\tau}*SSI \approx 4.08$ m is the gauge length. Using the time-differentiated phase change, the longitudinal strain rate $\dot{\mathcal{E}}_{xx,x}$ of the fiber section can be determined as follows :

$$\dot{\mathcal{E}}_{xx,x} = \frac{\lambda_0}{4\pi n_g \zeta L_G}\Delta\dot{\phi_x} \tag{8}$$

19

where ζ is the strain-optic coefficient that can be defined as:

$$\zeta = 1 - \frac{n_g^2}{2}[P_{12} - \nu(P_{11} + P_{12})] \tag{9}$$

where ν the Poisson's ratio of the fiber material and P_{11} and P_{11} are the Pockel photoelastic constants([21] Bertholds A. and Dandliker R., 1988; [12] Hartog, 2017; [3] Taweesintananon K. and Landrø M., 2021). $\zeta \approx 0.78$ was used for the silica fiber in this experiment. A constant ζ might lead to confusion that ends up to a false conclusion, as the time-differentiated phase change will only be considered as a function of the longitudinal deformation of the fiber according to (Equation 8), however, the strain-optic coefficient is implicitly affected by the fiber's longitudinal and transverse deformations. Integrating the strain rate along time axis result in the longitudinal strain ($\mathcal{E}_{xx,x}$) of the fiber section as follows :

$$\mathcal{E}_{xx,x} = \int_0^1 \dot{\mathcal{E}}_{xx,x} dt \tag{10}$$

The time-differentiated phase change data were recorded and calculated by extracting only 10,5000 channel sampled at every 2.04 m from 0 to 21 km from the optical circulator.

5.2   Strain effects on the optical fiber

The phase of the light in radians can be defined as follows:

$$\phi = 2\pi \left(\frac{L_0}{\lambda_0}\right) \tag{11}$$

where L_0 and λ_0 are the optical path length and wavelength in free space, respectively. The optical path length can be defined as follows:

$$L_0 = n_g L = \left(\frac{c}{v_{ph}}\right) L \tag{12}$$

where L is the distance traveled by the light inside the zone in which the interference effects are observed, and c is the speed of light in vacuum, and v_{ph} is the speed of light in the fiber. The relative change of an optical path can be written as:

$$\frac{\Delta L_0}{L_0} = \mathcal{E}_L - \frac{\Delta v_{ph}}{v_{ph}} \tag{13}$$

Where $\mathcal{E}_L = \Delta L/L$. The two-way propagation of a backscattered light along the fiber axis is L ≈ 2x, and by considering a linearly polarized beam and dismiss the the fiber birefringence, it was found that the optical strain is approximately equal to the longitudinal strain $\mathcal{E}_L \approx \mathcal{E}_{xx} = \Delta x/x$. By considering a light with a constant wavelength, the optical path change can be used, as it is the main contributor to phase change, to rewrite the phase change across the gauge length ($x = L_G$) as follows:

$$\Delta\phi = \frac{2\pi}{\lambda_0}\Delta L_0 \approx \frac{4\pi n_g L_G}{\lambda_0}\left(\frac{\Delta L_o}{L_0}\right) \tag{14}$$

The dielectric tensor of the fiber controls the phase velocity of light. Pockel constants can be used to describe (Equation 13) for a uniform and isotropic material ([23]Bakku, 2015)

$$\frac{\Delta L_o}{L_0} = \mathcal{E}_{xx} - \frac{n_g^2}{2}[(P_{11} - P_{44})\mathcal{E}_\perp + P_{12}\mathcal{E}_{xx}] \tag{15}$$

where $P_{12} = P_{11} - 2P_{44}$ and $\mathcal{E}_\perp$ is the transverse fiber strain, using the parameter introduced by([22] Kuvshinov, 2016), we can rewrite (Equation 15) as follows:

$$\frac{\Delta L_o}{L_0} \approx 0.7\mathcal{E}_{xx} - 0.2\mathcal{E}_\perp \tag{16}$$

Which means the final DAS signal calculated based on phase change method is the strain contribution from all directions.

The transverse fiber strain depends on the longitudinal strain , for a very tiny transverse stress, by the Poisson effect ([22]Kuvshinov, 2016) :

$$\mathcal{E}_\perp = \mathcal{E}_{\perp,1} + \mathcal{E}_{\perp,2} \approx -2\nu\mathcal{E}_{xx} \tag{17}$$

In this context, we can conclude that the physical longitudinal strain controls the relative change of the optical path in a fiber as follows

$$\frac{\Delta L_0}{L_0} \approx \zeta\mathcal{E}_{xx} \tag{18}$$

This proportional relation in (Equation 18) represents the basis of all practical DAS applications and it is the most accepted by the scholars.

5.3   DAS directivity

The amplitude of a seismic wave usually decreases with time due to numerous reasons, for example, spherical divergence causes amplitude loss, as the amplitude of the seismic wave traveling from a point source to a receiver decreases linearly with the travel distance (r), inelastic attenuation is also responsible for amplitude losses in the form of heat due to the friction between the seismic wave and the surrounding media, reverberations is also affecting the seismic wave amplitude ....etc. Different factors contribute to and affect the amplitude response from DAS, among and the most important of these factors are the source and the receiver directivity. The propagating strain field can be described in terms of a harmonic source with the accompanying ghost combined with the spherical divergence effects as follows:

$$\mathcal{E}_{rr} = \frac{1}{r}\left[2sin\left(\frac{2\pi f z_s}{v}cos\phi\right)\right]\mathcal{E}_{source} \tag{19}$$

where $\mathcal{E}_{source}$ is the strain field from a seismic source, f is the frequency, z_s is the source depth, v is the wave velocity in water and ϕ is angle between the wave propagating direction and the vertical axis, according to (Figure 11) ([24] Drijkoningen, 2003), the square bracket term in (Equation 19) is related to the directivity of the source with the ghost associated.

For the direct wave travels from source to the DAS cable, we are more concerned with the P-wave that when it impinges the cable, as inherited property of P-wave, it will produce a strain in the same direction of the wave propagation direction. Now, the propagating strain is ($\mathcal{E}_{rr}$) that results from a planar P-wave that propagates along the r-axis that forms the grazing angle (θ) with the straight cable along the x-axis as shown in (Figure 11). By analysing the resulting strain, the strain component projection onto the cable axis will be as follows:

$$\mathcal{E}_{xx}^{(c)} = \mathcal{E}_{rr}cos^2(\theta) \tag{20}$$

whereas, its projection onto the perpendicular direction to the cable is equal to:

$$\mathcal{E}_{\perp}^{(c)} = \mathcal{E}_{rr}sin^2(\theta) \tag{21}$$

([22] Kuvshinov, 2016) studied the anisotropic physical properties of a straight optical fiber coated by an elastic filler. Assuming a perfect coupling between the cable and the fiber, the isostrain loading condition is formed as a result of the longitudinal deformation of the cable and fiber in response to longitudinal forces, in this case, the strain is preserved, as the transportation of the longitudinal strain $\mathcal{E}_{xx}$ from cable to the fiber happens perfectly, unaccompanied by any losses such that:

$$\mathcal{E}_{xx}^{(f)} = \mathcal{E}_{xx}^{(c)} \tag{22}$$

the superscripts (f) and (c) refers to the fiber and cable, respectively. In the contrary, the isostress loading condition is formed from the forces normal to the cable axis, such that; $\sigma_{\perp}^{(f)} = \sigma_{\perp}^{(c)}$. This way, the fiber's transverse strain can be defined as follows:

$$\mathcal{E}_{\perp}^{(f)} = \left(\frac{E^{(c)}}{E^{(f)}}\right)\mathcal{E}_{\perp}^{(c)} \equiv \alpha\mathcal{E}_{\perp}^{(c)} \tag{23}$$

where $\alpha = E^{(c)}/E^{(f)}$, which reflects the transformation efficiency of the transverse strain from a cable to the coated fiber. $\alpha = 1$ when both the fiber and the coated material (cable) are made of the same material, however, the coating material has a lower effective Young's modulus than the coated fiber , and by combining equation 16 and strain relations from the previous equations, relative change of an optical path in DAS varies with the grazing angle can be defined as follows:

$$\frac{\Delta L_0}{L_0} \approx 0.7\mathcal{E}_{xx}^{(f)} - 0.2\mathcal{E}_{\perp}^{(f)} = (0.7cos^2(\theta) - 0.2\alpha sin^2(\theta))\mathcal{E}_{rr} \tag{24}$$

Now we can deduce that the point strain is directly controls the average strain at a DAS channel, which is related to the optical path change within the DAS array response such that:

$$A_{DAS} = \left[\frac{sin\left(\frac{k_x L_G}{2}\right)}{\frac{k_x L_G}{2}}\right]\left[\frac{sin\left(\frac{k_x L_w}{2}\right)}{\frac{k_x L_w}{2}}\right]\left(\frac{\Delta L_0}{L_0}\right) \tag{25}$$

L_G and L_W is the gauge length and the pulse width respectively and k_x is the angular wavenumber along the fiber axis. Having a grazing angle θ gives, $K_x = kcos(\theta) = (2\pi f/v)cos(\theta)$. Equation 25 to be rewritten as :

$$A_{DAS} = \left[\frac{sin\left(\frac{\pi f L_G}{v}cos(\theta)\right)}{\frac{\pi f L_G}{v}cos(\theta)}\right]\left[\frac{sin\left(\frac{\pi f L_w}{v}cos(\theta)\right)}{\frac{\pi f L_w}{v}cos(\theta)}\right]\left(\frac{\Delta L_0}{L_0}\right) \tag{26}$$

where f and v are the frequency and velocity of the wave, respectively. Now obtaining the total directivity of the DAS system for a marine seismic survey can be done by combining the response of the source and receiver arrays from equations 19, 24 and 26 as follows :

$$\begin{aligned}A_{Total-DAS} &\approx \left[\frac{sin\left(\frac{\pi f L_G}{v}cos(\theta)\right)}{\frac{\pi f L_G}{v}cos(\theta)}\right]\left[\frac{sin\left(\frac{\pi f L_w}{v}cos(\theta)\right)}{\frac{\pi f L_w}{v}cos(\theta)}\right]\\ &* (0.7cos^2(\theta) - 0.2\alpha sin^2(\theta))\\ &* \frac{1}{r}\left[2sin\left(\frac{2\pi f z_s}{v}cos\phi\right)\right]\mathcal{E}_{source}\end{aligned} \tag{27}$$

5.4   Shot position determination

As it was mentioned before, The DAS data set lacks the shot position, instead, ([3] Taweesintananon K. and Landrø M., 2021) introduced an intelligent method to determine the distance between the source and the cable according to (Figure 11). A relation between t_0, which is the UTC time when the source is fired, and t, which is the UTC time that represents the arrival time of the direct wave, and τ, which is the source to receiver traveltime, can be defined as:

$$\tau = t - t_0 \tag{28}$$

The travel distance of the direct wave from source to the receiver with respect to an online offset h_x can be calculated as flollows:

$$v\tau = \sqrt{d^2 + h_x^2} \tag{29}$$

where d is the source to cable distance. Thus, it is possible to rewrite the direct wave traveltime as a function of the inline offset h_x as follows:

$$\tau_{\{h_x\}} = \frac{1}{v}\sqrt{d^2 + h_x^2} \tag{30}$$

Traveltime has a minimum at the receiver with a zero inline offset ($h_x = 0$) such that

$$\tau_{\{h_x=0\}} = \frac{d}{v} \tag{31}$$

Thus, the traveltime difference between the zero inline offset and an arbitrary offset can be defined as follows:

$$\Delta\tau = \tau_{\{h_x\}} - \tau_{\{h_x=0\}} = \frac{1}{v}\sqrt{d^2 + h_x^2} - \frac{d}{v} \tag{32}$$

Equation 2 can be obtained by simple rearrangement of equation 32 as follows:

$$\Delta\tau + \frac{d}{v} = \frac{1}{v}\sqrt{d^2 + h_x^2} \tag{33}$$

$$\left(\Delta\tau + \frac{d}{v}\right)^2 = \frac{1}{v^2}(d^2 + h_x^2) \tag{34}$$

$$(\Delta\tau)^2 + 2(\Delta\tau)\left(\frac{d}{v}\right) + \frac{d^2}{v^2} = \frac{d^2}{v^2} + \frac{h_x^2}{v^2} \tag{35}$$

$$d = \frac{v}{2\Delta\tau}\left(\frac{h_x^2}{v^2} - (\Delta\tau)^2\right) \tag{36}$$

5.5 DAS processing workflow

SHEARWATER REVEAL package (version: 4.1) was used in this study as the main processing software. Starting with the raw DAS data, we went through a processing workflow in order to produce an image of the subsurface that is capable of revealing the subsurface features. The processing work flow went as follows :

5.5.1 Data upload

The DAS data consists of 3000 file in segy format. By using the Input tool, the data was successfully uploaded to SHEARWATER REVEAL software package.

5.5.2 Processing grid creation

It is necessary to create processing grid at first. A 'crooked line' geometry was selected and an offset bin spacing of 1 m was used

5.5.3 Data sorting

Use the Input tool for sorting on FFID and CHANNEL. The HeaderSetup tool can be used to compute the MPT-X and MPT-Y and CMP headerwords.

5.5.4 Static correction and QC

Static correction provides a mean to overcome variations in travel time between different sources and receivers due to variation in positions. A static correction have been applied to our data set to redatum the source and recievers to the sea surface using the following equation:

$$Correction = \frac{SRC_{(Depth)}}{v} + \frac{REC_{(Depth)}}{v} \tag{37}$$

where $SRC_{(Depth)}$ and $REC_{(Depth)}$ refer to source depth and reciever depth respectively, and v refers to the wave velocity in water.

5.5.5 Band-pass Filtering

The raw DAS data has been affected by high frequency noises, that masked almost most of the subsurface features. Applying a Band-pass of order 140 Hz/20 dB - 850 Hz/20 dB will be effective to improve the resolution through discarding these noises, to reveal some of the subsurface features.

5.5.6 Deconvolution

Deconvolution has been applied to our data set, Deconvolution is a filtering that removes a wavelet from the recorded seismic trace by reversing the process of convolution. Deconvolution is performed along the time axis to increase temporal resolution by compressing the basic seismic wavelet in the recorded seismogram and attenuating reverberations and short–period multiples.

5.5.7   Autocorrelation

Autocorrelation has been applied to the data set and analyzed as well. Autocorrelation provides substantial information used to determine the deconvolution parameters and to evaluate the quality of deconvolution outputs. Analyzing the autocorrelation function, recurring events, such as long- or short-period reverberations, in the seismic data can be determined. Long-period reverberations usually appear as isolated amplitude packages in the autocorrelation series.

5.5.8   Velocity analysis and NMO correction

Normal Moveout (NMO) represents the difference in travel time that results from varying ray path lengths. Correction for this NMO will correct the traveltime from arbitrary offsets to zero offset. In this study, NMO correction has been applied for two different events independently :

- First, The direct arrivals travelled directly from the seismic source to the DAS receivers on the seafloar using water velocity of 1500 m/s.

- Second, the Rreflected waves from the underlying geological structure through velocity analysis.

Seismic velocity analysis aims to evaluate optimal NMO (or stacking) velocity to provide the best focusing of seismic data. Usually, it is done by computing semblance from the data with various velocities being applied in normal moveout correction. From the data sorted in midpoint-offset coordinates U(m,h,t), the velocity semblance S(m,t_0,t) should be computed , where $(m = (X_r + X_s)/2)$ and $(h = X_r - X_s)$ and optimal velocity is found from the maximum of semblance, $(V_{nmo}(m,t) = max_v S(m,h,t))$. The velocity anomalies are wider for large values of (t_0) and large velocities. It means that the accuracy of velocity analysis decreases with (t_0) , reflection moveout becomes less senistive to change in velocity.

Reveal provides a good tool for velocity analysis. A velocity flow was created and velocities were picked from maximum semblance and then the flow was run to complete the velocity analysis for the reflected data.

5.5.9   Muting and Stacking

A muting has been applied to the undesired NMO stretched data at far offsets, followed by stacking to the NMO corrected data. having many traces in a CMP can improve the quality of the image, as stacking (sum) the traces for a given CMP will result in :

- Noise cancels out.

- Real signal (geology) is amplified.

- Signal to noise ratio increase

5.5.10 Stacks combination

Combining the two stacks, the direct and the reflected stacks, together results in a zero-offset seismic reflected common stack.

5.5.11 Post stack time migration

A post stack time migration has been applied to our data set.

5.5.12 Final Filtering

A final band-pass filter has been applied to the data at 180 Hz/20- 450 Hz/20 dB.

5.6 Streamer processing workflow

The streamer processing workflow is different from the one that has been applied previously with the DAS data due to the fact that the streamer data comes from a single channel streamer. Starting with data uploading, processing grid creation and sorting the data in FFID/CHANNEL, our processing workflow continued as follows:

5.6.1 Static correction and QC

Although the source and streamer depths approximately one meter below the sea surface, we have applied a static time correction, to redatum them to the sea surface, to correct even for any small changes in depths.

5.6.2 Direct wave elimination

As there is no benefit might be gained out of the direct wave from the streamer. Elimination has been applied to the direct wave travelled directly from source to receivers.

5.6.3 NMO Correction

It was not applicable to apply velocity analysis based on a single channel streamer data to determine the stacking velocity. Instead, we have used the stacking velocities that have been extracted from the DAS data to apply NMO correction for the streamer data.

5.6.4 Deconvolution and Autocorrelation

Autocorrelation has been applied before and after deconvolution to check the effectiveness of the application of the deconvolution to the streamer data.

5.6.5   Zero-offset time migration

Using the velocity model from the DAS data, a zero-offset time migration has been applied to the streamer data.

5.6.6   Final band-pass filter

A band-pass filter of order 150 Hz/20- 400 Hz/20 dB has been applied to the streamer data as a final step.

6 Results

The results section is subdivided into three parts. Results of the DAS amplitude analysis will be presented first, that will help giving us a clear understanding of the DAS directivity, however, DAS processing workflow used for imaging of the subsurface of the Trondheimsfjord will be presented in the second part. Finally, imaging from the processed streamer data will be presented in the last part.

6.1 DAS Amplitude Analysis

Different factors contribute to the ultimate amplitude results from DAS, However, among the most important factors that have a major contribution to the final amplitude results are the source directivity and the DAS cable directivity.

6.1.1 Source Directivity

Understanding the source sensitivity to the the propagation angle is so crucial. Almost all marine seismic sources are accompanying with source ghosts, as a result it is important to take into account ghost effects on the amplitude as well.
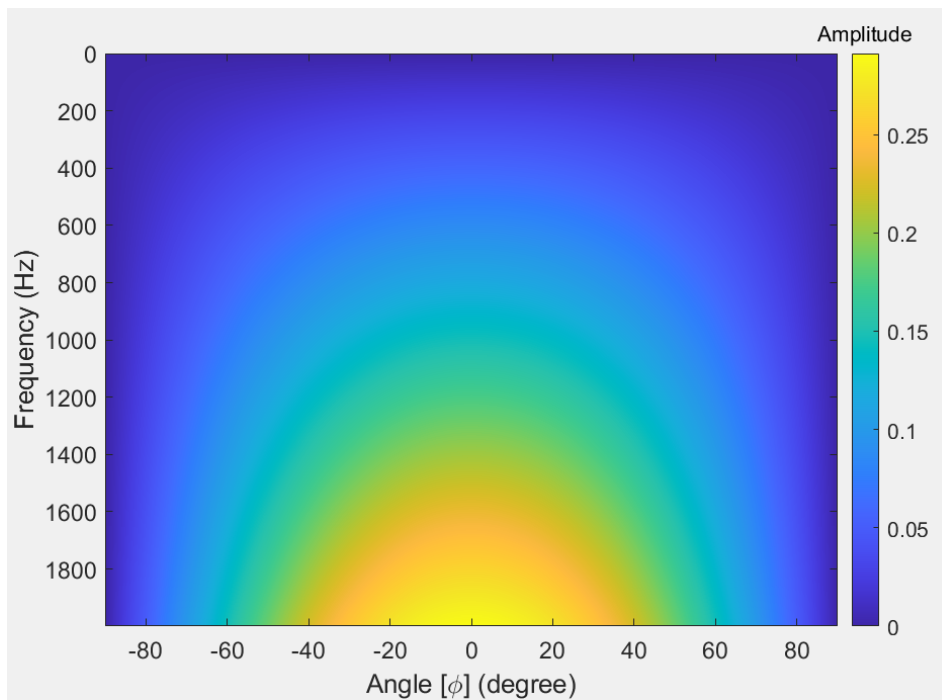
Figure 18: Amplitude Directivity of a harmonic point source with the accompanying ghost, Notice, maximum amplitude is reached around ($\phi = 0^0$) from the vertical. Water velocity of 1500 m/s and source depth of 1 m below sea surface have been used.

Using equation [19], the amplitude from a harmonic point source and the accompanying ghost has been modeled as a function of the propagation angle $[\phi]$, according to (Figure 11), and frequency. Water velocity of 1500 m/s and source depth of 1 m below sea surface have been used in our calculations. Notice, the ghost effects is corresponding to the square bracket in equation [19]. The result can be seen in (Figure 18).

As it can be noticed from the (Figure 18), the the propagation angle $[\phi]$ has a major control on the amplitude from a point source, and the maximum amplitude is achieved around the normal incidence $(\phi = 0^0)$, and it starts to decrease gradually as $[\phi]$ increases. Moreover, the source ghosts effects result in decreasing the overall amplitude compared to a case if the source is ghost free.

6.1.2   DAS array Directivity

The second factor to be considered is the DAS array sensitivity to the angle of incidence. The DAS array response has been modeled according to equation 26, as a function of frequency and the incidence angle $[\theta]$, according to (Figure 11), where a water velocity of 1500 m/s and a gauge length (L_G) which is equal to the pulse width $L_W = 4.08$ m were used in our analysis, and the result of the analysis can be seen in (Figure 19).
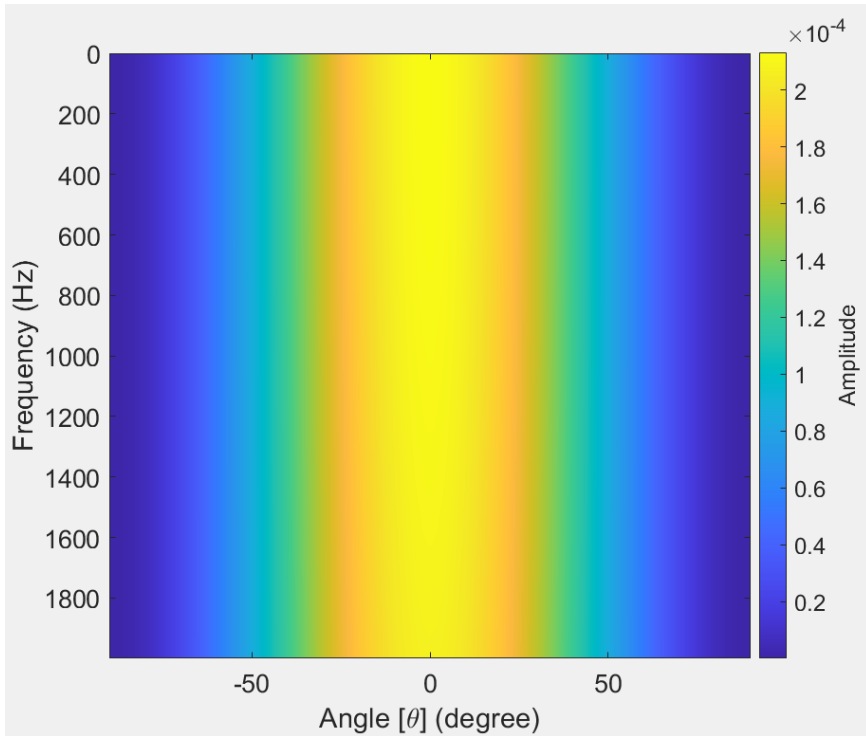
Figure 19: DAS array response as a function of the incidence angle $[\theta]$ and frequency. Water velocity of 1500 m/s has been used. Notice, maximum amplitude is achieved at horizontal incidence $(\theta=0^0)$.

As it can be seen from the analysis, the incidence angle (θ) controls the DAS array response, where the maximum amplitude is reached when the incidence angle is around the horizontal incidence ($\theta = 0^0$), parallel to the cable direction. On the other hand, the amplitude tends to decrease gradually as the incidence angle approaching the normal incidence ($\theta = 90^0$). Another notice is that the DAS array response hasn't been affected much by changing the frequency of the incident wave, that might indicate that frequency change alone is not enough to cause a phase shift, that the interrogator can detect.

6.1.3 Total DAS Directivity

Modelling the ultimate DAS response requires combining the point source directivity with the DAS array directivity. This has been done using (Equation 27) to model the total DAS directivity as a function of frequency and the incidence angle [θ]. The same previous values for the variables were used, and the result can be seen (Figure 20).
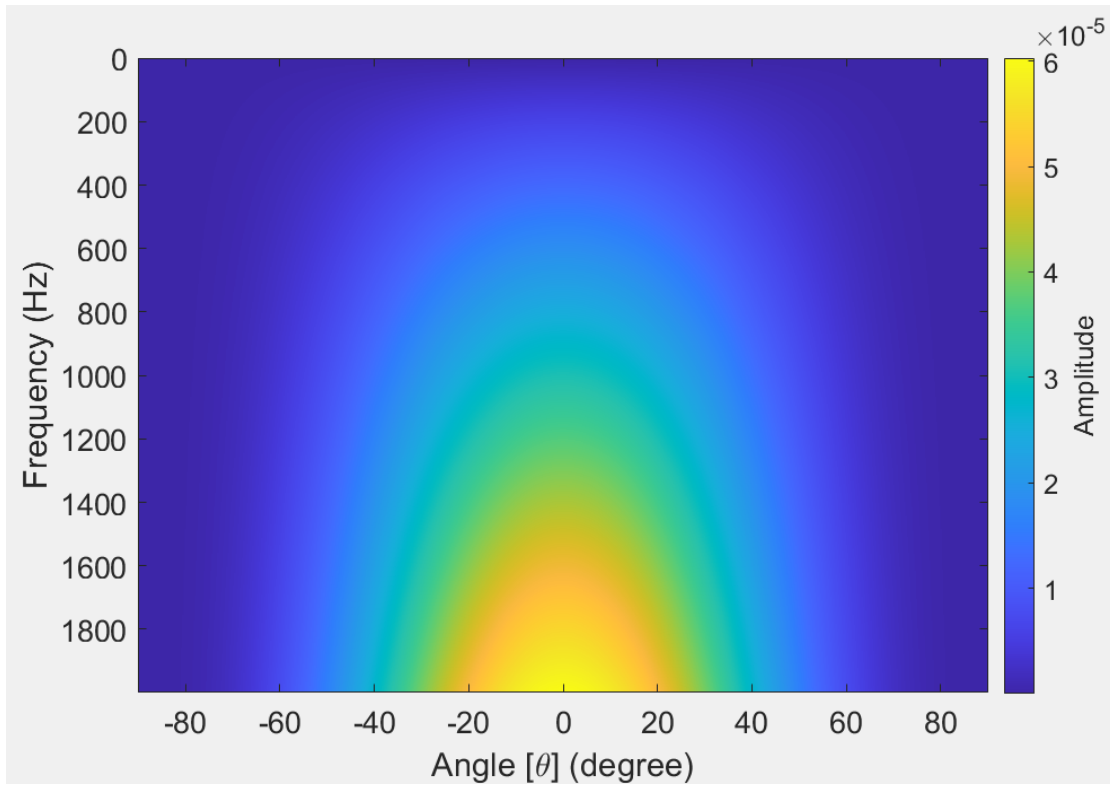
Figure 20: Total DAS array response modelled using (Equation 27) , notice the recorded amplitude is much smaller compared to the initial source amplitude due to the DAS directivity, the spherical divergence effects is excluded in this model.

Notice the total DAS amplitude response has a lower amplitude compared to original amplitude from the source, due to combining the DAS array sensitivity to the angle of

incidence (θ) and the source sensitivity to the angle of propagation (ϕ), as the maximum amplitude at DAS array around ($\theta = 0$) will encounter a lower amplitude from source, where (ϕ) is around 90^0.

The ultimate amplitude from DAS has been modeled using two different values of the coupling coefficient (α), zero and one respectively, where $\alpha = 1$ when the cable and fiber are made from the same material, Results can be seen in (Figure 21). As it can be seen from the model, when the coating material (cable) and fiber are made from the same material, the signal will show a polarity reversal to a small negative values as we approaching the normal incidence angle ($\theta = 90^0$). However, in reality the coating material is often made from a material that is different from the material from which the fiber is made. As a result, it might be acceptable to consider the case when ($\alpha = 0$) as a reference model to compare our real DAS amplitude analysis to it.
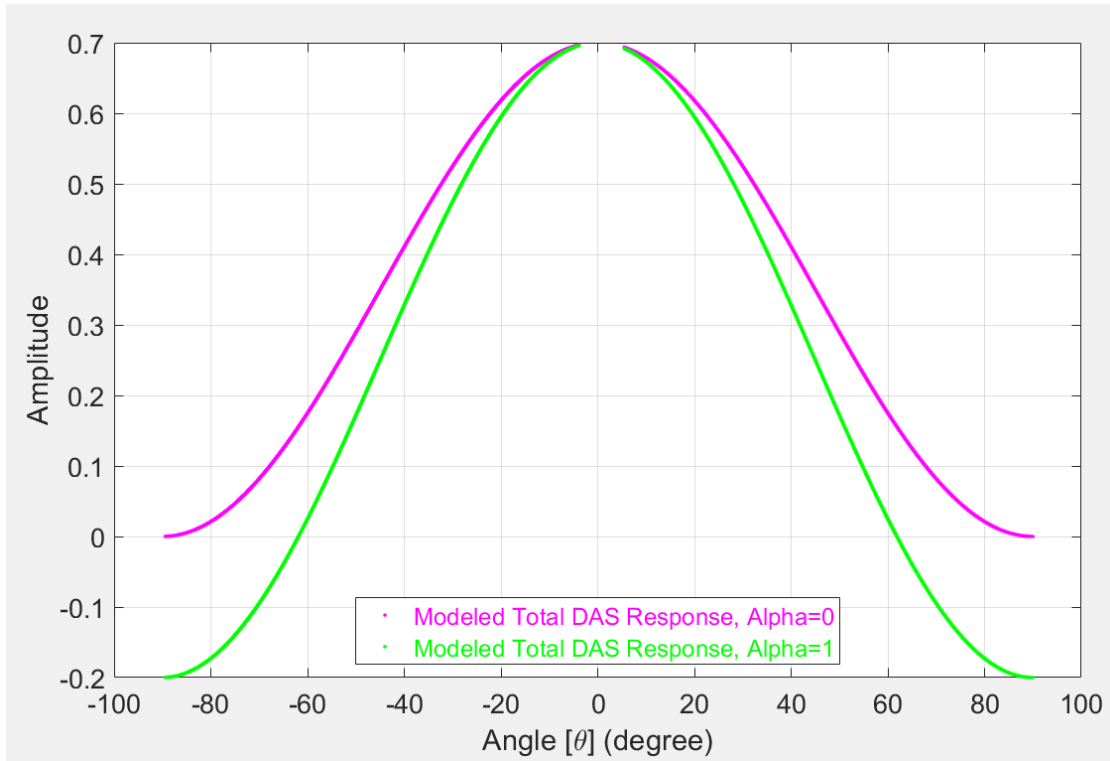
Figure 21: Modeled total DAS amplitude using two different vales for α. Notice the green curve, when $\alpha = 1$ has been used, the amplitude shows a polarity reversal when approaching the normal incidence $\theta = 90^0$.

6.1.4   DAS Amplitude analysis from the Trondheimsfjord

In this study, DAS amplitude analysis from the Trondheimsfjord has been done using the direct arrivals. NMO has been applied to the direct arrivals from a common channel

gather of channel number 452, using water velocity of 1500 m/s to bring them back as if the source and receiver are directly above each other, see (Figure 22). We noticed that the direct arrivals don't show up in all shots, only limited number of shots can provide a good signal to be used for the amplitude analysis. As a result, a window of 2 ms has been chosen for the amplitude analysis, at which we manually picked the top of this window, to be sure that it includes the complete response from the direct arrivals, the top of this window is marked by the red line shown in (Figure 22).

Another observation is that, the signal is not perfectly flat, even after the NMO correction. One possible explanation might be due to an incorrect data geometry might be used while setting the shot positions, as our study lacks the exact shot positions, and a straight DAS cable has been assumed to determine the relative shot positions to the DAS cable, however, in reality the cable might not be perfectly straight, moreover, it might include some local kinks.
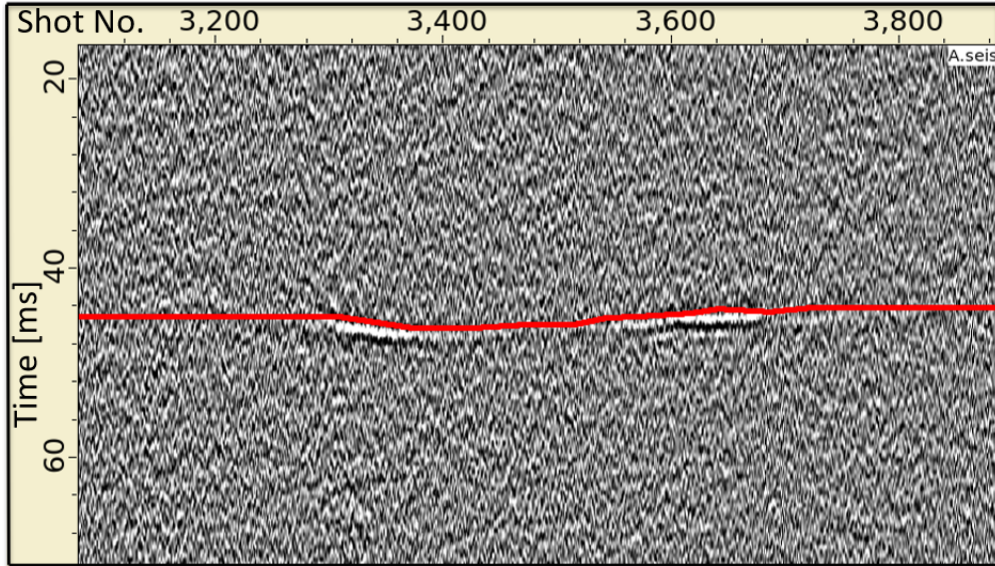
Figure 22: Common channel gather of channel number 452. Notice the NMO corrected direct arrivals are not perfectly flat. The red line represents the start line of a window of 2 ms for the amplitude analysis.

After using the amplitude analysis tools in SHEARWATER REVEAL. The result of the real DAS amplitude analysis of the direct arrivals from a common channel gather, channel number 452 versus the modeled total DAS amplitude using $\alpha = 0$ are plotted over each other as a function of the incidence angle $[\theta]$ and results can be seen in (Figure 23).

From our analysis to the amplitudes from this common channel gather, we can see that the real amplitudes are following the same trend as the model, to increase gradually as the incidence angle $[\theta]$ decreases. However, it is not perfectly overlay the model. One

33

possible explanation might be due to incorrect geometry used due to lacking of the exact shot positions, that surely will affect the final amplitudes due to the sensitivity of the DAS to angles, and all angles are calculated according to the these relative positions of shots to the DAS cable. However, results still agree with the model and do not contradict it.
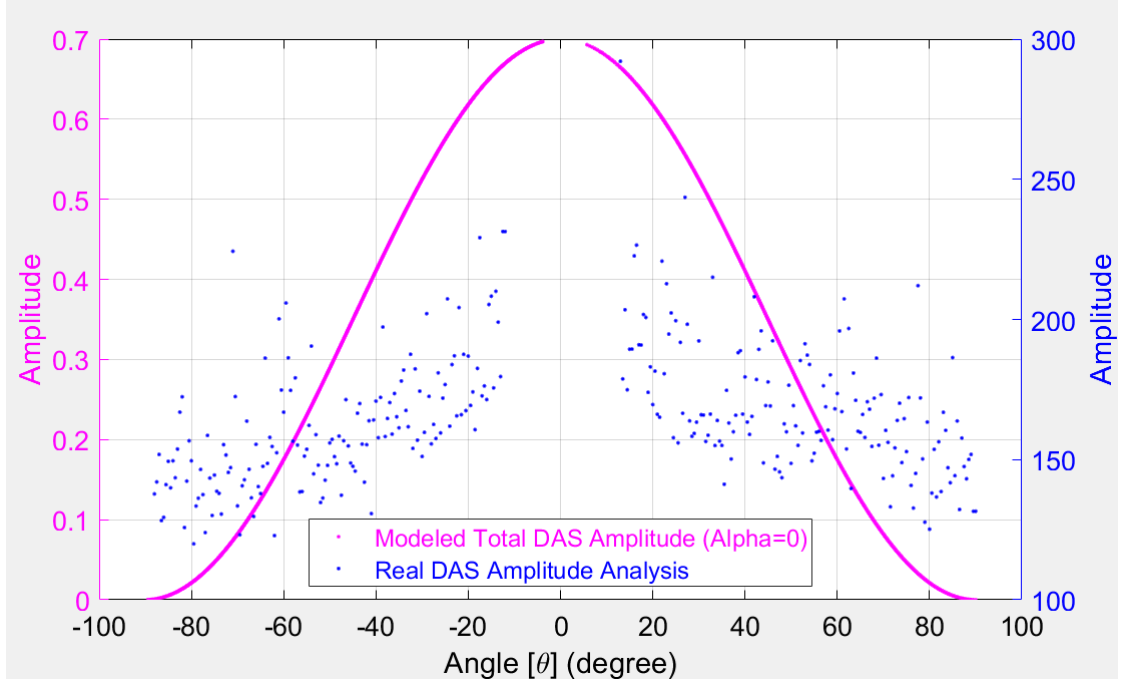
Figure 23: Real DAS amplitude analysis from a common channel gather, channel number 452 versus modeled total DAS amplitude using $\alpha = 0$. Notice, the real amplitudes increase gradually as $[\theta]$ decreases, however, they don't perfectly obey the model.

6.2   Subsurface imaging using DAS data from the Trondheimsfjord

We have followed the DAS processing workflow that has been previously discussed in the method section, and results that have been obtained are presented as follows.

6.2.1   Band pass filtering of the DAS data

After redatuming the source and the DAS cable to the sea surface, it was so notorious that the DAS data has been affected by high frequency noises, see (Figure 14), that masked most of the subsurface features. To discard these kind of noises, a band - pass filter of order 140 Hz/20 dB - 850 Hz/20 dB has been applied to our data, which has proven its effectiveness to improve the quality of the data by attenuating these noises, as it can be seen in (Figure 24). Moreover, The hyperbolic shape in the same figure that represents the direct arrivals, that have travelled directly from the seismic source to the

DAS cable, has become more visible as compared to (Figure 14), However, most of the reflections from subsurface geological structure still invisible in shot gather even after applying the band-pass filter.
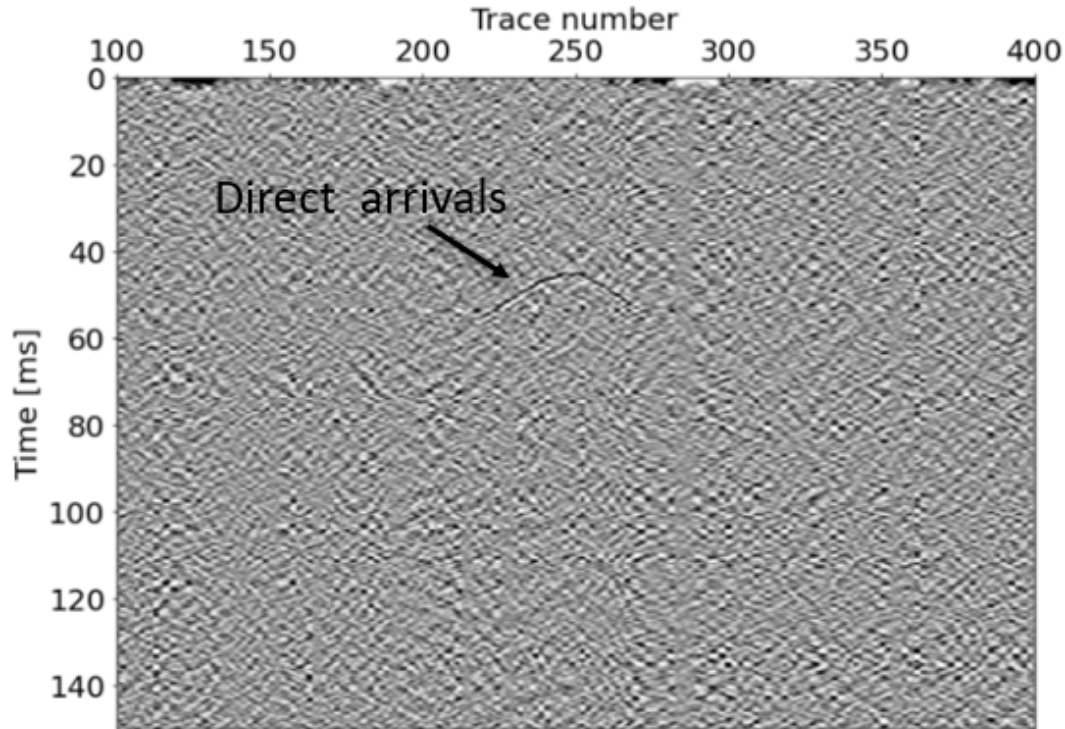
Figure 24: Band - pass filter of order 140 Hz/20 dB - 850 Hz/20 dB has been applied to the DAS data. Notice the hyperbolic shape that represents the direct arrivals of waves travelled directly from the seismic source to the DAS cable, become more visible and noises were eliminated successfully.

Usually these kind of noises are generated due to natural causes like oceanic waves..etc. However, as the noises have higher frequencies in our data set than normal, they might be generated due to imperfect tuning of the seismic source used in the study.

6.2.2   Velocity analysis and NMO

SHEARWATER REVEAL provides effective tools for seismic velocity analysis. (Figure 25) shows an example for a velocity analysis flow for CMP number 175. Four probes can be seen from left to right; top left shows the hyperbolic trend of each time-velocity pick. The next shows the semblance cloud for the current CMP gather, where the vertical red line is the velocity trend. The third probe is the gather with the normal moveout correction applied together with the horizontal line at the time of each pick. The top right probe is the constant velocity stack. A velocity model is generated automatically

after running of the velocity flow, see(Figure 26). The velocity model shows consistency in most parts of the model. However, it shows a a small inconsistency between CMP 400-500, which is equivalent to positions around 2600-2750 m, where a sudden sharp decrease in velocity followed by increase in velocities again, which might indicate incorrect velocities was used between these two points. One possible explanation might be due to incorrect geometry used, another possible reason might be due to the narrow a azimuth acquisition, as DAS might not be able to illuminate the structure and a wide a azimuth will give more possibility for the incident wave to hit the cable in a small angle of incidence $[\theta]$, at which the DAS is more sensitive.
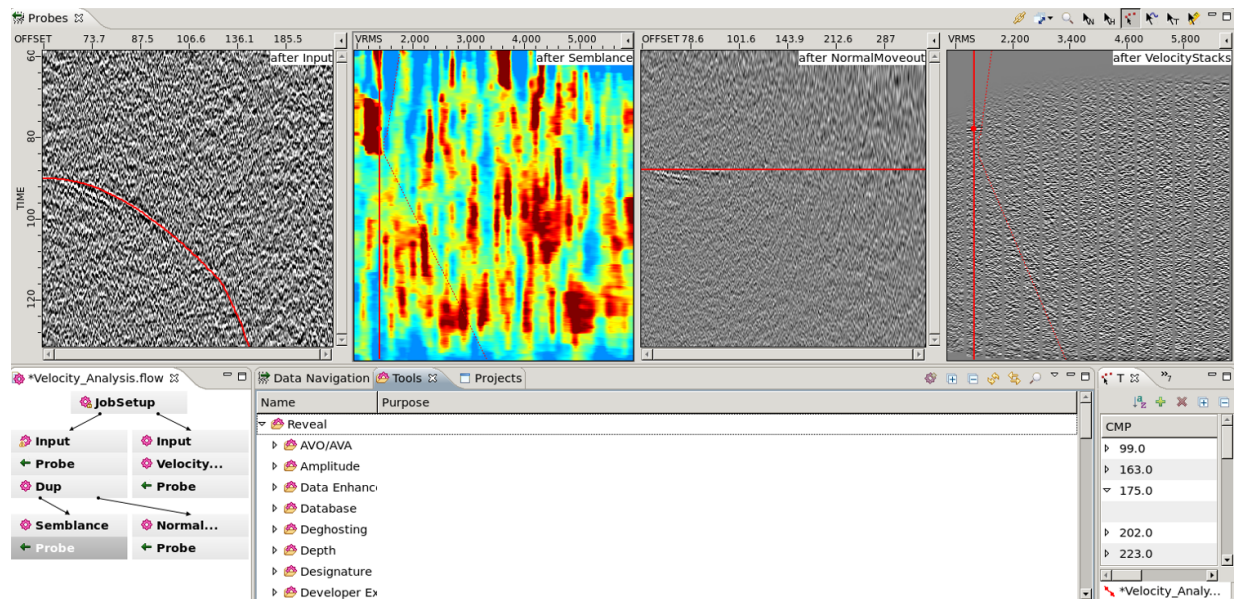
Figure 25: SHEARWATER REVEAL's velocity analysis flow of CMP number 175

As we are dealing with very shallow section, the time difference between the direct arrivals and reflections is too small. As a result, when trying to use the NMO velocity model of reflection data to stack the section, it will cause the direct arrivals to be under corrected due to using higher velocity of the reflected wave, and vice versa. As a result, we decided to do the NMO correction separately for both the direct arrivals and reflected waves.

6.2.3   Muting and Stacking

In this study two stacks were generated independently after NMO correction has been applied for both the direct arrivals and the reflected waves. The first stack was generated from the direct arrivals, however, the second one from the reflected waves. A constant water velocity of 1500 m/s has been used for normal move out correction for the direct arrivals, and a mute has been applied to the data with severe NMO stretch at far offsets

then a stack for the direct arrivals has been generated by summing all traces from the same CMP, see (Figure 27)
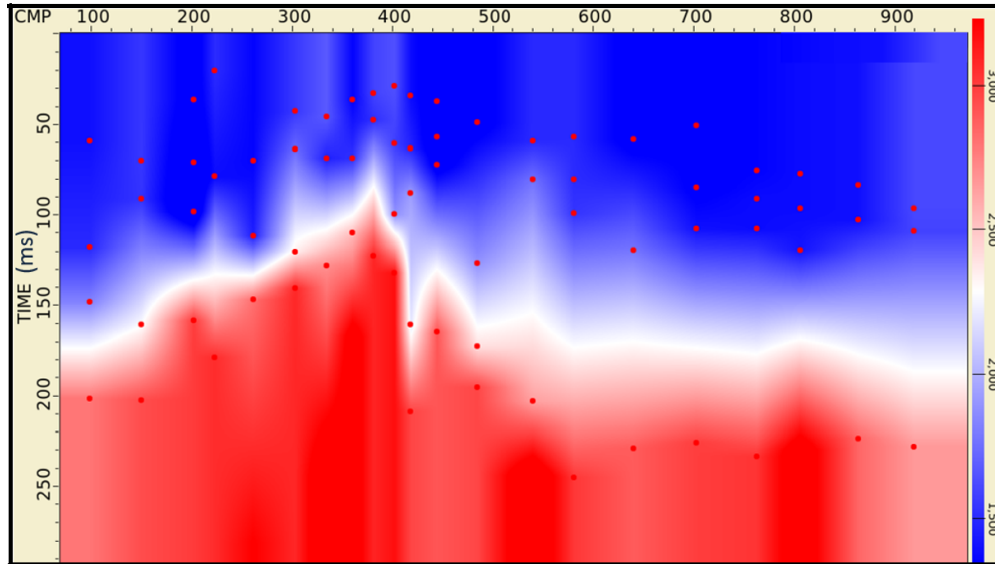
Figure 26: The velocity model used for NMO correction and stacking of the reflected waves.

It is interesting that the direct arrivals from DAS can be used to get information about the see floor topography as the DAS cable already is placed on the see floor at 0-2 m approximate depth. As it can be seen from the direct stack, reflections between positions around 2600-2750 m are not easy to follow. This might be due to the presence of kinks in the DAS cable between these two points or in correct geometry used. Another possible explanation might be that DAS was not able to properly illuminate this side of the seafloar due to the steep seafloar slope and a narrow azimuth acquisition was used. And wide azimuth acquisition might be helpful to image this part of the seafloar clearly , at which the DAS is more sensitive to small angle of incidence [θ].

On the other side, The velocity model used for the NMO correction and stacking of the reflected waves are obtained by time-velocity scanning semblance analysis as discussed before see (Figure 26). The output of the reflected stack can be seen in (Figure 28). Notice, the reflection stack shows strata that exists directly below seafloar, that have almost the same slope trend as the seafloar from the direct stack. This agreement between results even both stacks were generated independently, gives more confidence in the method used in this study. However, reflectors between position 2600-2750 m are not easy to follow, as the case in the direct stack.
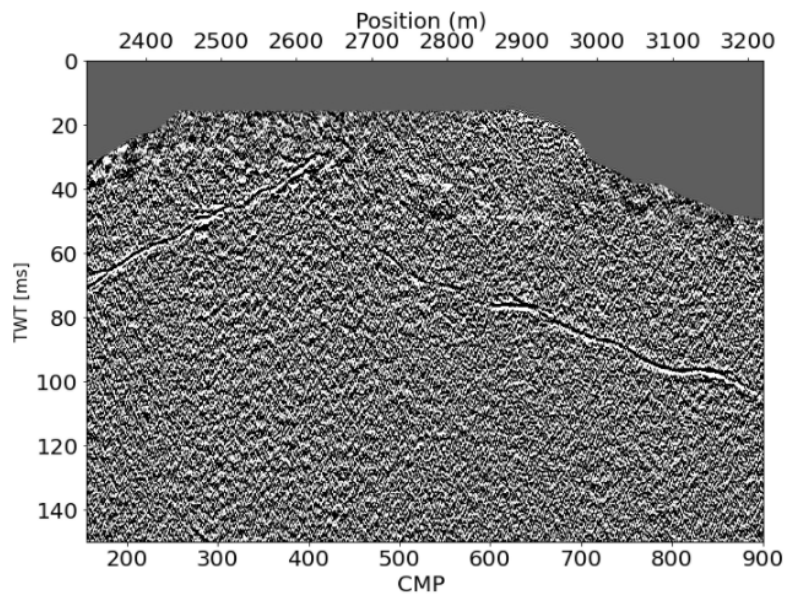
Figure 27: The Direct arrivals' stack was generated after using water velocity of 1500 m/s to NMO correction of the direct arrivals, notice the seafloar topography can be figured out from the direct arrival stack here.
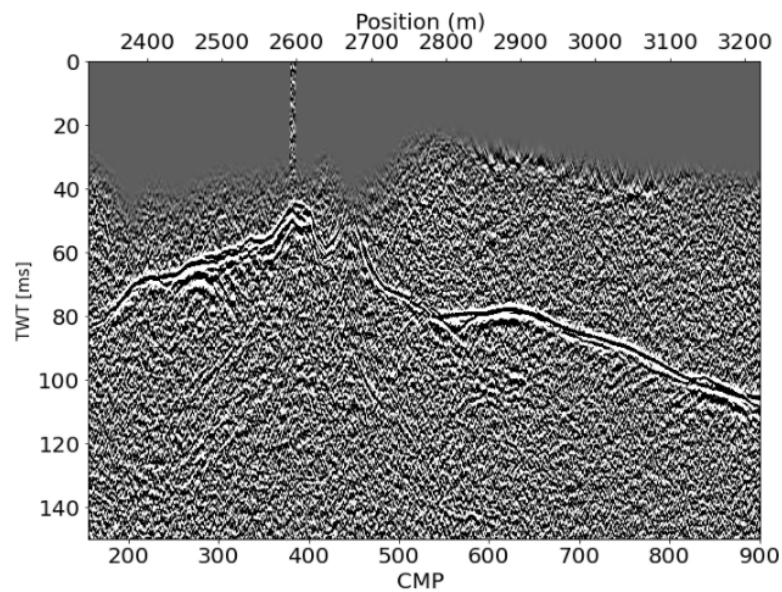
Figure 28: Reflected stack generated after NMO correction of the reflected waves using the velocity model (Figure 26) generated by time-velocity scanning semblance analysis.

6.2.4   Combine Stacks

In order to get a full image that includes both the direct arrivals and the reflected subsurface feature, a combined stack has been created by summing the traces from the same CMP from both stacks, see (Figure 29)

As it can be seen from the combined stack , there are two main features that can be figured out easily, marked by (1) which represents the direct arrivals that reflects the seafloor topography and (2) which represents reflections from the top of the bed rock. Notice, both events almost overlap each other starting from around CMP number 600, this indicates that the sediment thickness is small at these areas.
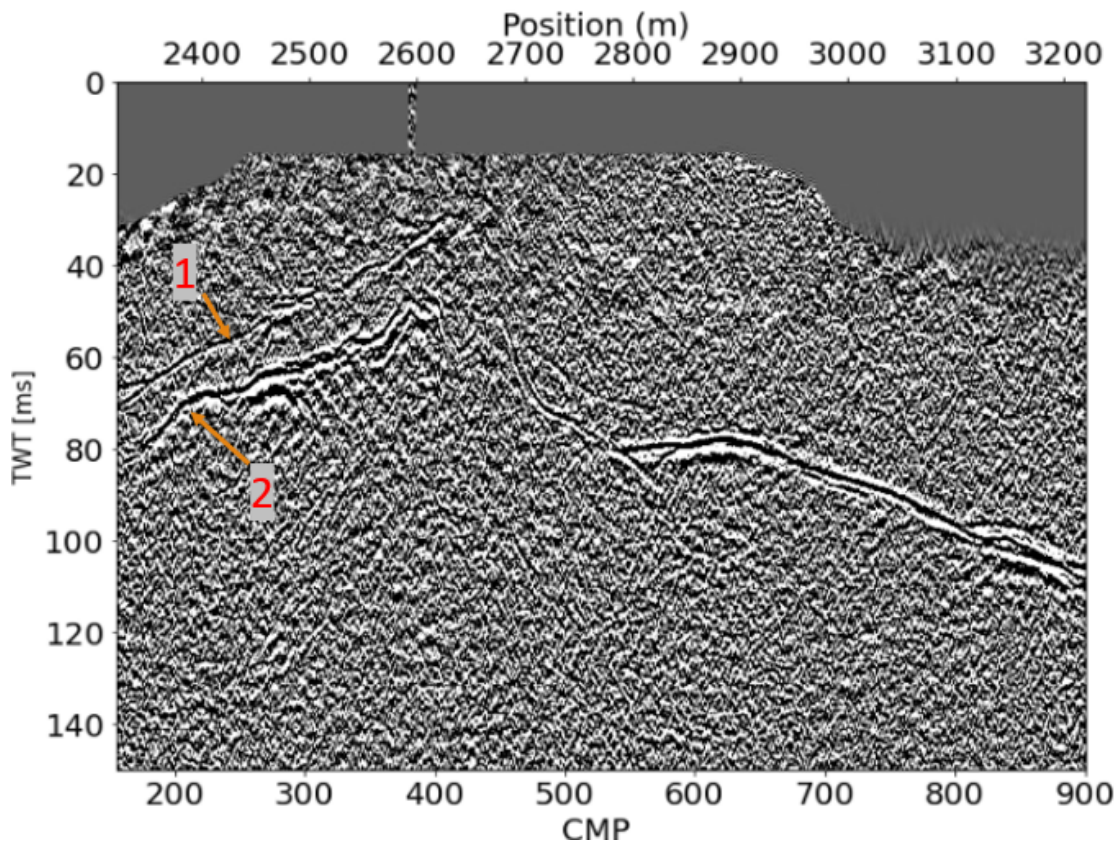
Figure 29: Combined stack including the direct arrivals marked by (1) representing the seafloor and (2) representing the top basement reflections. Notice the lower part of the figure has chaotic reflections from the basement.

Moreover, the frequency difference between the direct and reflected waves can be noticed easily, as the reflected waves has a lower frequency content than the direct waves, that might indicate that the absorption factor is quite high even for very small differences in

depths between the direct and reflected waves here. For the lower part of the section, the resolution of the section is low, might be due to the fact that most of the reflections from this part come from the basement. However, even with this low resolution in the lower part, some disrupted inter-basement reflections still can be recognised.

One other thing to notice from the combined stack that the DAS data still has a lower quality that characterised by faint, disrupted reflections between positions 2600-2750 m as discussed before.

6.2.5   Post stack time migration

Using the velocity model created by velocity analysis (Figure 26), a post stack time migration has been applied to our data set, see (Figure 30), However, the results from this step does not introduce significant improvements to the image, and most of the lower part of the section still blurry with no clear continuous reflections. This might be due to the fact that our seismic section is shallow and the stacking velocity may be already correct, that the migration will not add much to the image.
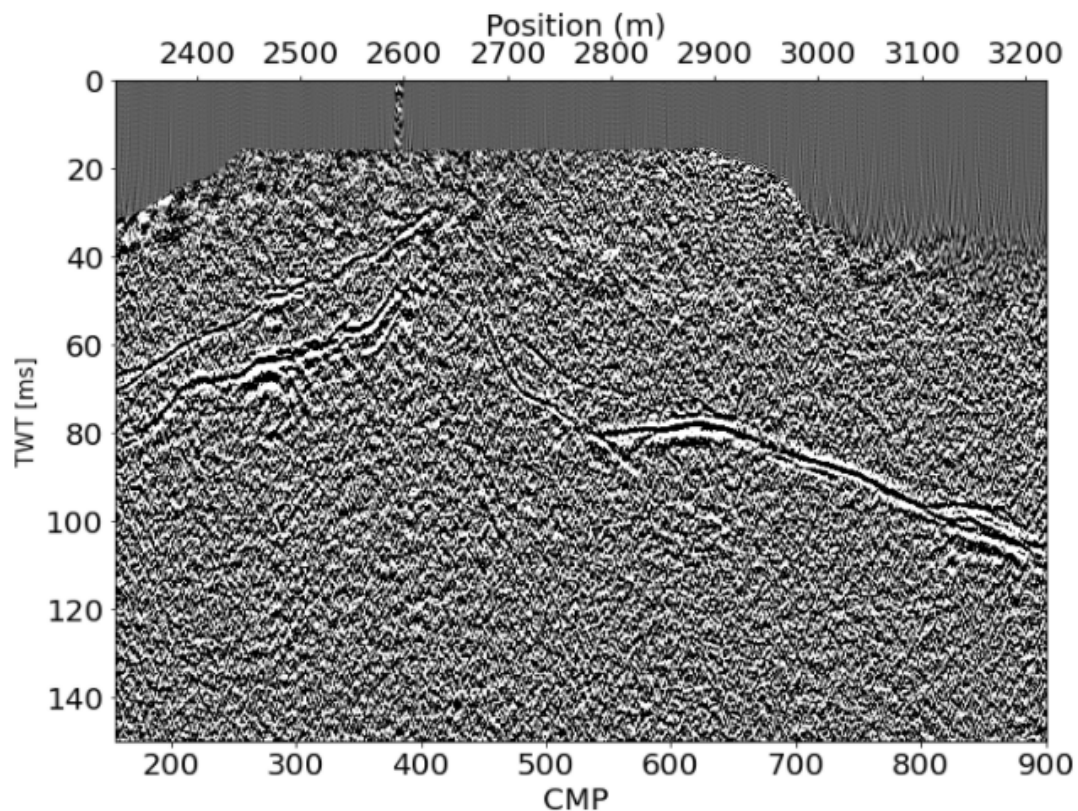
Figure 30: Post stack time migrated seismic section from DAS data.

6.2.6   Deconvolution and Autocorrelation

Deconvolution can improve the quality of the image by suppressing the source wavelet and removing the short period multiples, however, as it was discussed, it might introduce some artifacts as well. "Autocorrelation provides substantial information to determine the deconvolution parameters and to evaluate the quality of deconvolution outputs" ([26] Dondurur D., 2018) by checking the degree of correlations or similarity between nearby events. Autocorrelation has been applied to our data set both before and after deconvolution. As it can be seen from (Figure 31) autocorrelation after deconvolution provides better results indicating that the deconvolution was really effective in improving the quality of the data through eliminating the source wavelet and remove short period multiples.

Getting good results from the autocorrelation, encouraged to use the deconvoluted data to reproduce the direct stack, the reflected stack and the combined stack, to be compared with the previously generated stacks. A Comparison between direct stacks, reflected stacks and the combined stacks both before and after deconvolution can be seen in figures 32, 33 and 34 respectively. As it can be seen from these figures, deconvolution has improved the quality of the images, by introducing more sharp reflectors that has been reflected in a more clear image.

One thing to be noticed is that, despite the deconvolution has improved the shallow reflectors, it introduced more distortion to the lower part of the section, however, we neglected this side effect, in favour of having more clear reflections from the main reflectors.
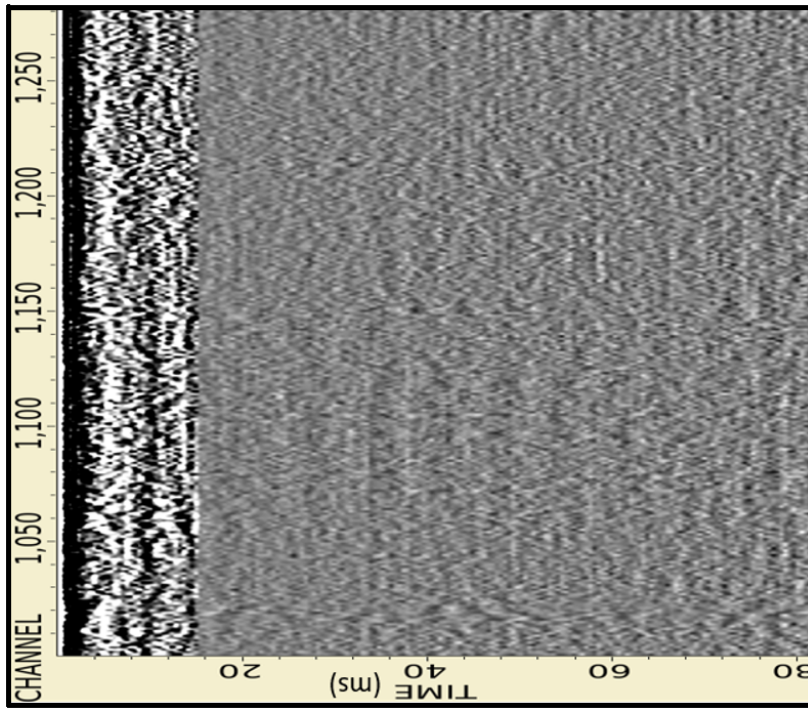
(b)
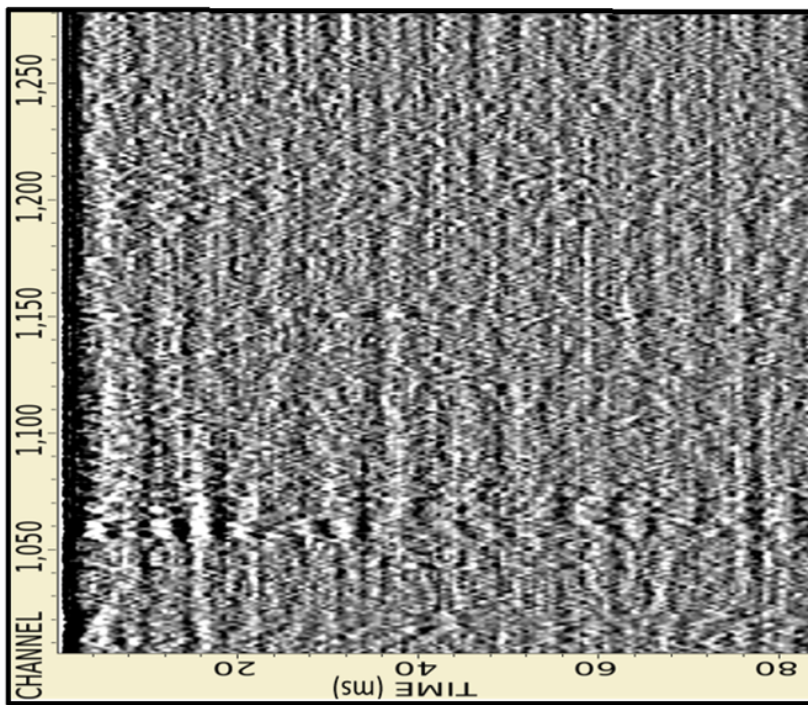
(a)

Figure 31: (a) Autocorrelation results of the DAS data before deconvolution, versus (b) Autocorrelation results after deconvolution. Notice the autocorrelation results are much better after deconcolution, which reflects the effectiveness of the deconvolution to improve the image quality.
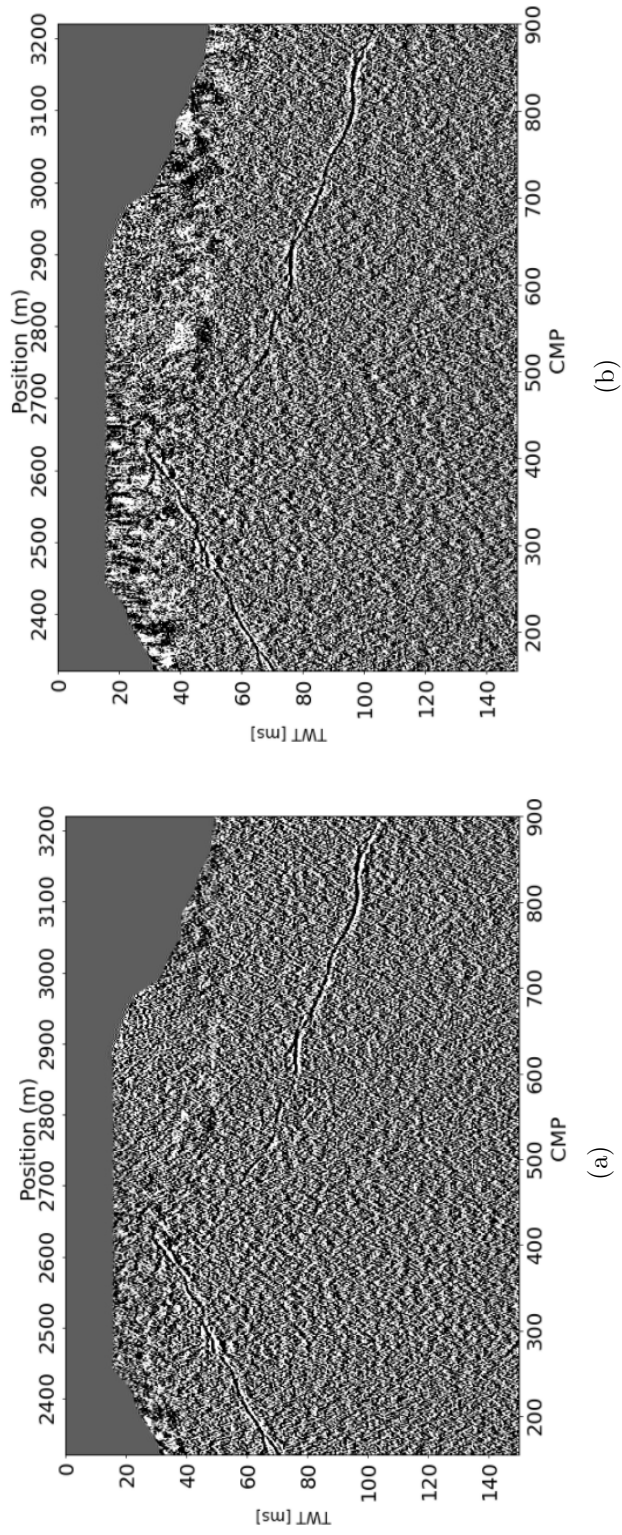
Figure 32: Comparison between (a) Direct stack before deconvolution and (b) Direct stack after deconvolution. Notice sharp reflections are obtained after applying the deconvolution.
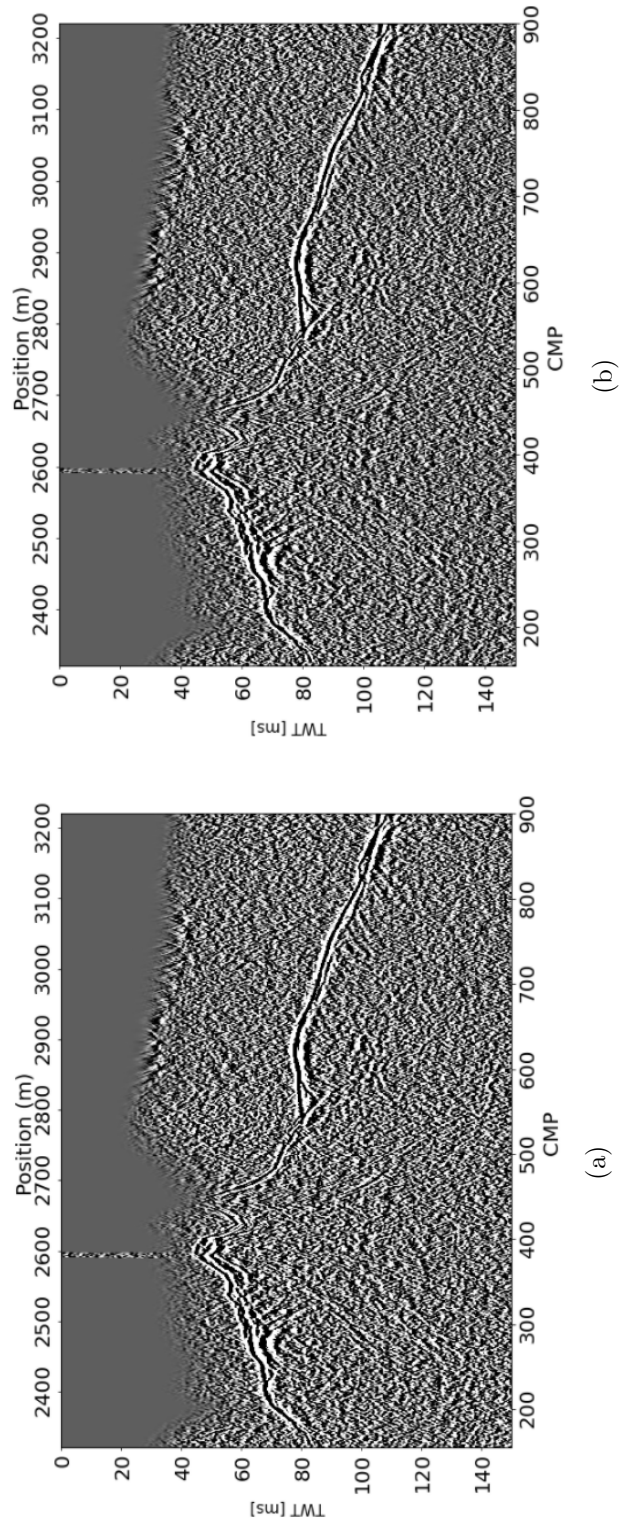
Figure 33: Comparison between (a) Reflected stack before deconvolution and (b) Reflected stack after deconvolution. Notice sharp reflections are obtained after applying the deconvolution.
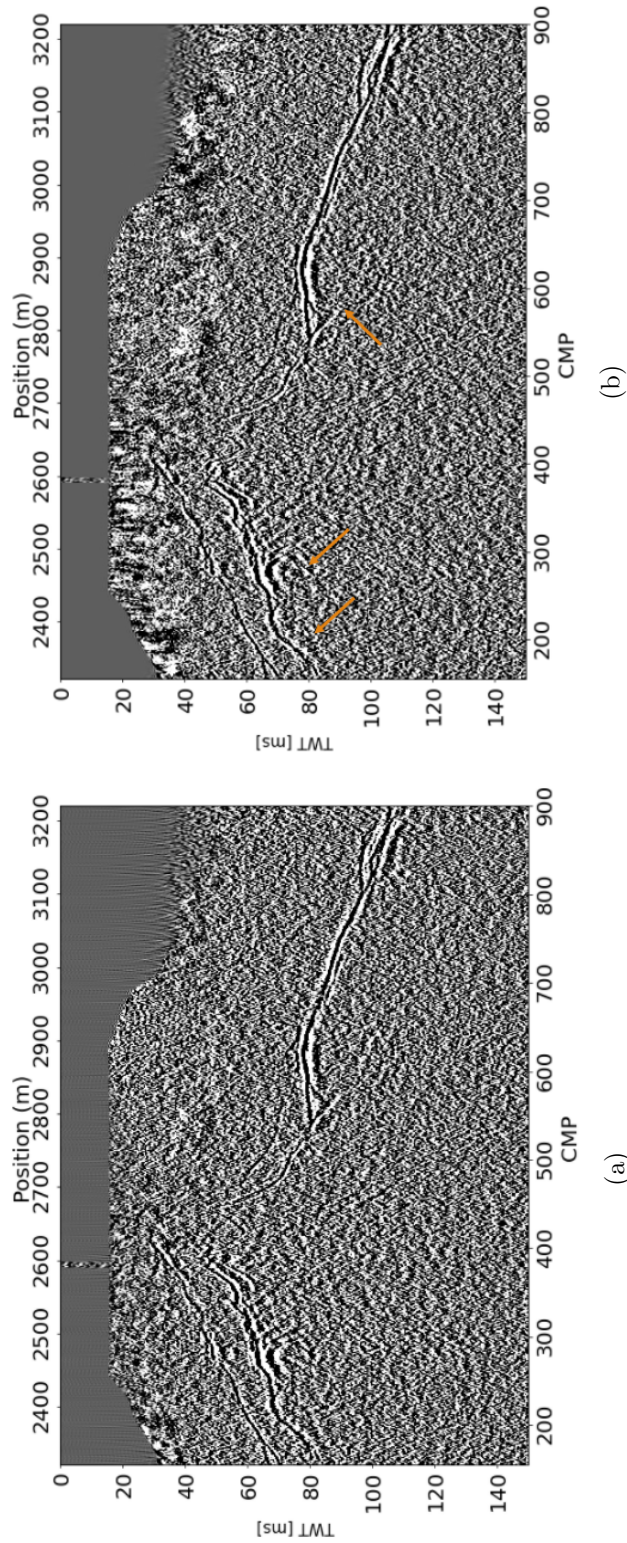
Figure 34: Comparison between (a) Combined stack before deconvolution and (b) Combined stack after deconvolution. Notice sharp reflections are obtained after applying the deconvolution, moreover, some reflectors marked by orange arrows, become more visible.

45

6.2.7 Final band-pass

A final band pass filter of order 180 Hz/20 dB - 450 Hz/20 dB has been applied to our data set, see (Figure 35), the filter has proven its effectiveness to improve the image quality, by removing undesired noises, this figure represents the final output from the planned DAS processing workflow, ending up with more clear reflections, except for the reflections between positions around 2600-2750 m.
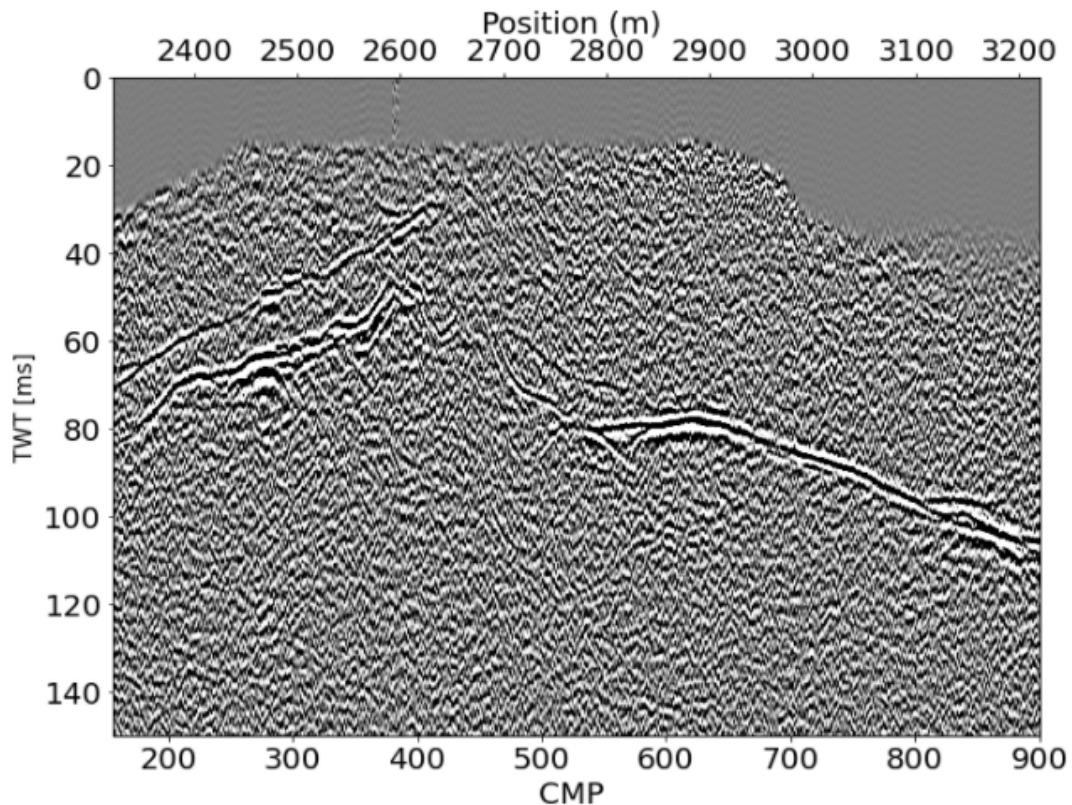
Figure 35: Application of a final band pass Filter of order 180 Hz/20 dB - 450 Hz/20 dB to DAS data. Notice the filter successfully improved the image quality, introducing more sharp and clear reflections, except for the reflections between positions around 2600-2750 m.

Three different possibilities might be responsible for these unclear reflections between positions 2600-2750 m as discussed before that can summarized as follows:

- DAS sensitivity to the incidence angle due to the narrow azimuth acquisition used and wide azimuth acquisition may solve the problem.

- Wrong geometry due to lacking of the exact shot positions.

- The presence of local kinks in the cable between these positions.

In order to limit the possible explanations for these unclear reflections, although the DAS data lacks the zero offset data, we tried to regenerate the stacks using the near offsets by selecting only the first 90 channels from each shot, as the near channels usually provide the strongest signals, to regenerate the stacks again, however, this might affect the data at the large offsets.

Near offsets were selected from the deconvoluted data, to regenerate direct stack, reflected stack and combined stack again and the same band pass filter of order 180 Hz/20 dB - 450 Hz/20 dB has been applied after post stack time migration has been applied using the velocity model (Figure 26) and results can be seen in figures 36, 37, 38 and 39.
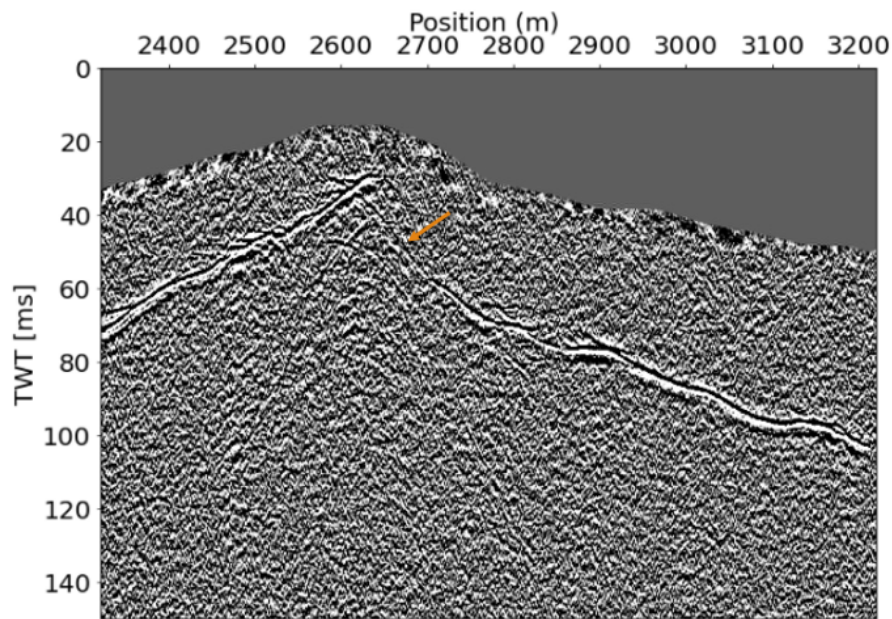
Figure 36: Direct arrivals stack generated by stacking data from near offset channels (The first 90 channels), notice the reflections become more continuous and can be followed, see the orange arrow.

Stacking data from near offset channels has achieved excellent improvements, that after the application of the final band pass, reflections from seafloor and top basement in the area that was poorly imaged using the normal stack, can be easily traced . As a result, we can deduce that the wrong geometry due to lacking the exact shot positions caused unfocused energy that was responsible for the poor imaging between positions 2600-2750 m.
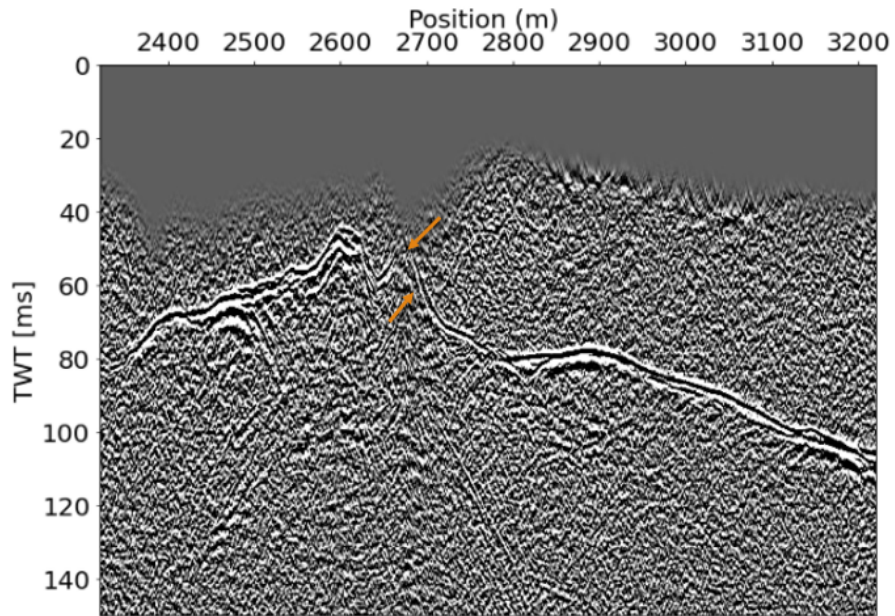
Figure 37: Reflected stack from near offset channels, notice the small improvement in the reflections although still disrupted.
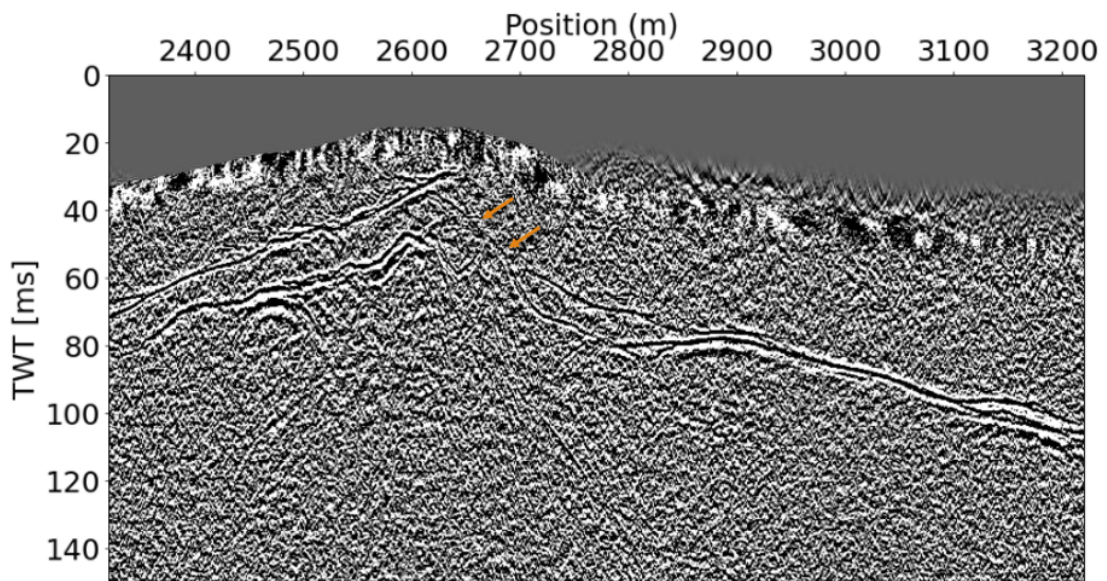
Figure 38: Combined stack from near offset channels, notice the great improvement in the seafloor continuity marked by orange arrows, however, the top basement reflector still not easy to follow.
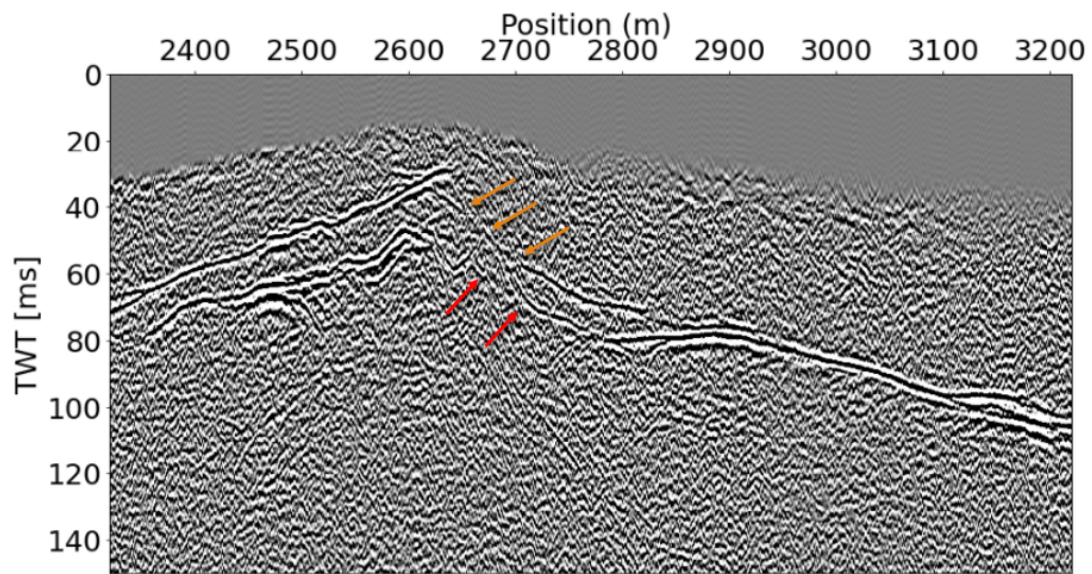
Figure 39: Final band pass of order 180 Hz/20 dB - 450 Hz/20 dB has been applied to data from near offset channels after applying post stack time migration , notice the great improvements in the reflectors continuity marked by orange arrows for the seafloor, and red arrows for the top basement.

6.3   Subsurface imaging using streamer data from the Trondheimsfjord

In order to check the quality of the generated image from DAS and judge the ability of the method to image the subsurface, it was so important to compare the results that have been obtained from DAS to results obtained from traditional marine seismic acquisition techniques. We followed the seismic processing workflow discussed before in the method section to process a single channel streamer data set that was acquired simultaneously with DAS data to be compared with each other.

6.3.1   NMO correction

The first step was to redatum the source and receivers to the sea surface. As the streamer data is obtained from a single channel, it was not applicable to apply velocity analysis based on a single channel data, instead, we used the velocity model calculated from the DAS data (Figure 26) to apply NMO correction for the streamer data. Moreover, In contrast to the direct waves from the DAS data that were used to get an indication about the seafloor topography, the direct wave travelled directly from the seismic source to the streamer has been eliminated, as it is considered here as a kind of noise, see (Figure 40).
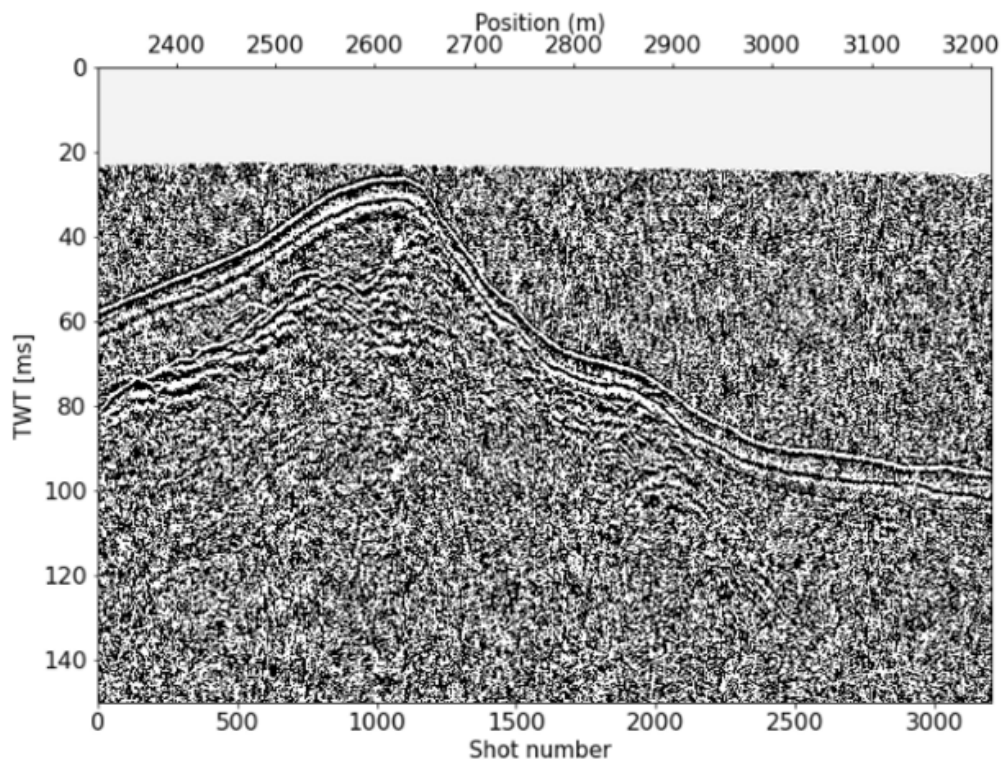
Figure 40: NMO corrected streamer data using the velocity model from DAS velocity analysis. Notice the direct wave has been muted.

6.3.2 Deconvolution and Autocorrelation

The application of Deconvolution to seismic data must be taken with caution, as it is possible for the deconvolution algorithms to cause distortion to the data and introduce some artifacts as well as discussed before. Autocorrelation has been applied to the streamer data both before and after deconvolution to evaluate the deconvolution ability to improve the quality of the image, see (Figure 41), however, the deconvolution here failed to achieve any improvements in the data quality that can be inferred from the result obtained from the autocorrelation. This might be due to failing to detect the true wavelet shape to be eliminated due to noises that might affected the wavelet shape. As a result, the deconvolution step has been skipped here.

(a)

(b)
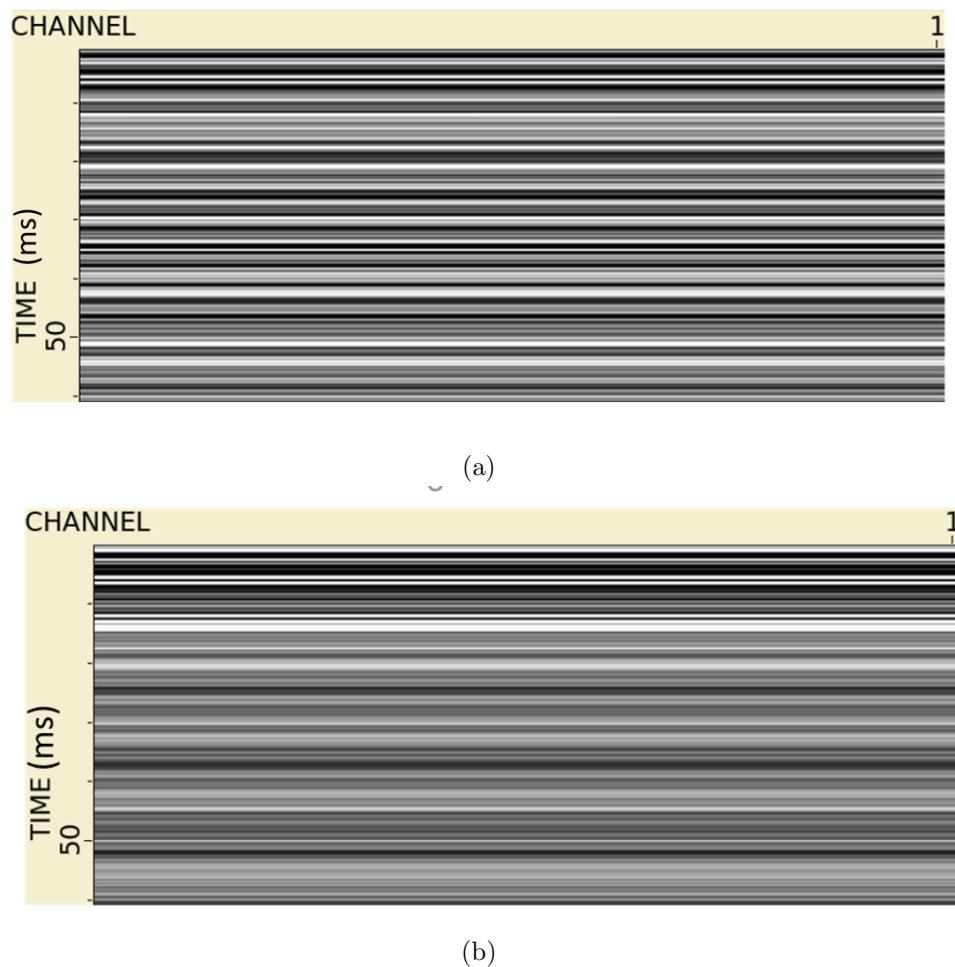
Figure 41: (a) Autocorrelation of the streamer data before deconvolution versus (b) Autocorrelation after deconvolution. Notice the deconcolution here failed to introduce improvements to the data.

6.3.3   Zero-offset time migration and Final band pass

Using the same velocity model from DAS, a zero-offset time migration has been applied to the streamer data followed by the application of a final band-pass filter of order 150 Hz/20 dB- 400 Hz/20 dB, results can be seen in (Figure 42).
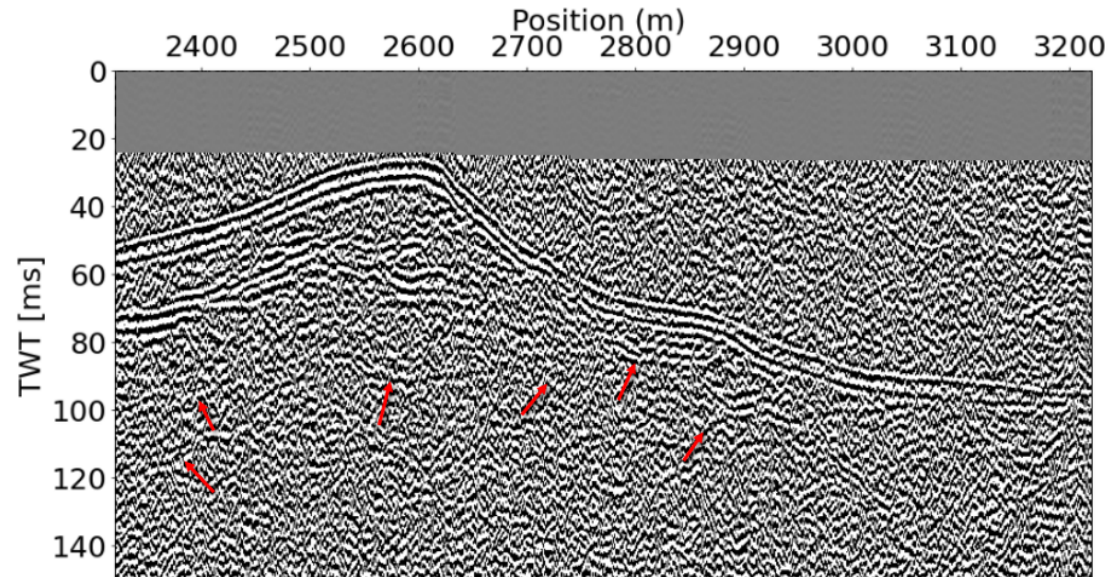
Figure 42: Band pass filter of order 150 Hz/20 dB-400 Hz/20 dB has been applied to the streamer data after zero-offset time migration. Notice the reflectors become more sharp and continuous after removing the undesired noises, notice the inter-basement reflectors, marked by red arrows.

The band-pass filter successfully improved the quality of the image introducing sharp, continuous reflectors leading to a high quality image. Notice, the there are some reflectors have become more visible inside the basement marked by the red arrows. This figure represents the final output image from the streamer data after applying the planned processing work flow.

7   Discussion

Traditional seismic acquisition techniques provide us a sophisticated mean for subsurface imaging. Nowadays, seismic imaging becomes an important tool used by the academia and the exploration community, helping them making better decisions in terms of the exploitation of the underground resources. However, these traditional seismic acquisition techniques cost exorbitant amount of money, that might limit the companies' abilities when it comes to investing more in exploration.

Searching for new techniques for seismic acquisition which is more cost effective is the best solution to cope with this issue. Distributed acoustic sensing (DAS) is one of the most promising technologies that might change the future of seismic acquisition. DAS transforms a submarine telecommunication cables into densely sampled seismic receivers which is more cost effective compared to the traditional acquisition techniques. The main task of this study was to test this new technique. First by testing its directivity. Second by conducting a seismic processing workflow which leads to producing an image of the subsurface of the Trondheimsfjord from DAS, and compare the results with results obtained from traditional streamer data that has been acquired simultaneously with DAS.

From our analysis to the DAS directivity, we have found that DAS is so sensitive to longitudinal strains, that a wavefield that impinges the cable in parallel to the cable orientation, will be easily sensed by DAS than a wave that hit the cable perpendicularly. That means according to (Figure 11) when the angle of incidence [θ] is zero, a maximum amplitude will be recorded by the interrogator. Moreover, the amplitude will gradually decrease as the incidence angle increases, see (Figure 19). This might be due to the fact that a wavefield that impinges the DAS cable perpendicular will fail to cause any phase shift between consecutive backscattered waves, as DAS is more sensitive to the longitudinal strain.

The source directivity affects the DAS resolution as well, as from the analysis of the source directivity, it has been figured out that the maximum amplitude from the source will be encountered at normal incidence, $\phi = 0^0$ according to (Figure 11) , see also (Figure 18). By combining the DAS array sensitivity to the angle of incidence (θ) and the source sensitivity to the angle of propagation (ϕ) (Figure 20), we figured out that the maximum amplitude at DAS array around ($\theta = 0^0$) will encounter a lower amplitude from source, where (ϕ) is around 90^0. As a result, a more energetic source should be used to increase the spacial resolution of the image, to make up for the amplitude loses due to the DAS directivity.

In order to generate an image of the subsurface from DAS data, we had to deal with the velocity analysis in a different way to perform the NMO correction in the correct way. It was a good idea to make use of the direct arrivals from DAS to get an idea about the seafloor topography, as the DAS cable already exist on the seafloor around 0-2 m approximate depth. However, we faced the reality that our seismic section is shallow and the time difference between the direct arrivals and underlying reflection is small,

at which using the velocities of the reflected waves for NMO correction will cause the direct arrivals to be undercorrected due to the use of higher velocities, and vice versa if velocities of the direct arrivals were used to apply the NMO correction for the reflected data. As a result, the NMO correction has been done independently for both the direct arrivals and the reflected data.

Using the deconvoluted data, first, a constant water velocity of 1500 m/s has been used for normal move out correction for the direct arrivals, and a mute has been applied to the data with severe NMO stretch at far offsets, then a stack for the direct arrivals has been generated by summing all traces from the same CMP. Secondly, The velocity model used for the NMO correction and stacking of the reflected waves was obtained by time-velocity scanning semblance analysis. The combination between the two stacks, the one from direct arrivals and the one from reflected data, was required to get a complete image of the subsurface from DAS. This has been done by summing the traces from the same CMP from both stacks.

Getting a combined stack from DAS, a post stack time migration has been applied, that followed by the application of a final band pass filter, it was notorious that the reflected data has a lower frequency content than the direct arrivals, which suggests that the absorption factor is high. Moreover, DAS was not able to fully illuminate the the structure between positions 2600-2750 m which makes it not easy to follow the reflectors between these positions. This might be due to the presence of kinks in the DAS cable between these two points or incorrect geometry used as our data set lacks the exact shot positions. Another possible explanation might be due to the DAS directivity as a narrow azimuth acquisition was used, and wide azimuth acquisition might be helpful to image this part of the structure. By stacking the near offset channels from each shot, we were able to image these disrupted reflectors, see (Figure 39), Thus we got a reasonable explanation for these unclear reflections, that lacking the exact shot positions introduced some error while setting the geometry, that was responsible for unfocused energy along the steep slope reflectors between positions 2600-2750 m.

The streamer data came from a single channel. First, the data has been redatumed to the sea surface, however, it was not applicable to apply the velocity analysis based on a single channel data, as a result, the velocity model from DAS was used to apply NMO correction to the streamer data. The direct arrivals have been eliminated and a zero-offset time migration has been applied using the same velocity model from DAS and a final band pass filter has been applied as well. A comparison between the final output images from both Distributed Acoustic Sensing (DAS) and the towed single channel streamer can be seen in (Figure 45).

The image production method was different for each image. For the image from streamer, only reflection data was used to generate the image. However, for the image from DAS, both the direct and the reflected waves were used to produce the image. Comparing the signal to noise ratio (S/N) from both DAS and streamer data shows that both of the DAS and the streamer data have comparable signal to noise ratio, see (Figure 43), however, in general the streamer data has a higher signal to noise ratio (S/N) than the

DAS Data. Figure (44) shows a comparison between the normalized power spectrum for both the DAS and the streamer data. From these comparisons, it becomes more clear that the DAS data has a lower frequency content than the streamer data.
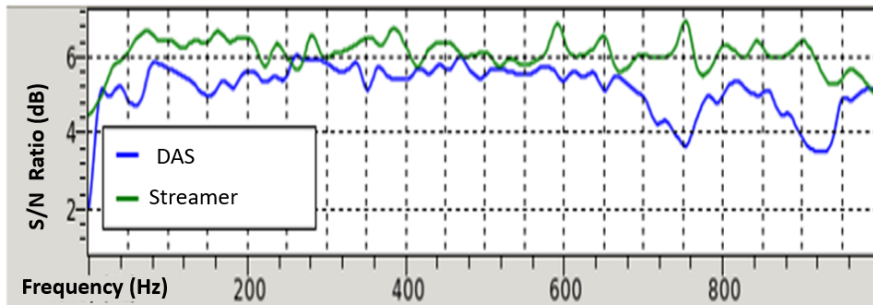
Figure 43: Comparison between the signal to noise ratio (S/N) for both streamer (blue) and DAS (green). Notice that both of DAS and the streamer has comparable signal to noise ratio.
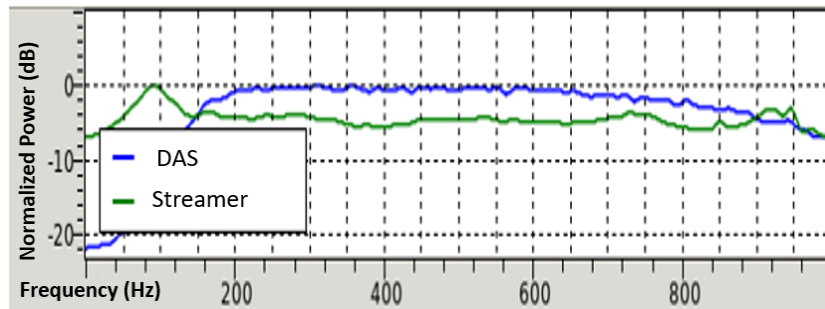
Figure 44: Comparison between the normalized power spectrum from both DAS and streamer data.

By comparing both images (Figure 45) , it can be easily figured out that the image from DAS has a lower frequency content and lower resolution, the early affection by the high frequency noises might added to the lower resolution that caused by the inexact shot positions, although the band pass filter successfully removed most of these noises, however, some of them may be still exist. On the other hand, the image from the streamer provides a more clear and obvious reflectors that can be easily traced and has a higher (S/N) ratio as well, this may be due to using densely spaced 24 hydrophone in a 7 m streamer length, which will result in a high (S/N) ratio.

Both methods were able to image the structure in the subsurface and the main reflectors, the seafloor and the top basement, can be traced. Moreover, some inter-basement reflectors can be compared from both methods, However, the base Holocene can't be seen from the DAS image, which is a boundary separating between bioturbated clay, silty, and sandy sediment and the deposits from unit two which comprises the glaciomarine sediments of Allerød and Younger Dryar.

Although the data from both methods were redatumed to the sea surface, however, there is small time shift between the main reflectors from both methods, that might be due to some error introduced by wrong geometry due to lacking the exact shot positions, another possible explanation might be due to the fact that both methods are looking to the structure from different locations. DAS has succeeded to image the subsurface under the Trondheimsfjord, Norway, however, the image from DAS can be improved by using a more powerful source and wide azimuth acquisition, decreasing the gauge length that will be helpful to increase the spacial resolution and using lower frequencies will increase the wave penetration inside the Earth.
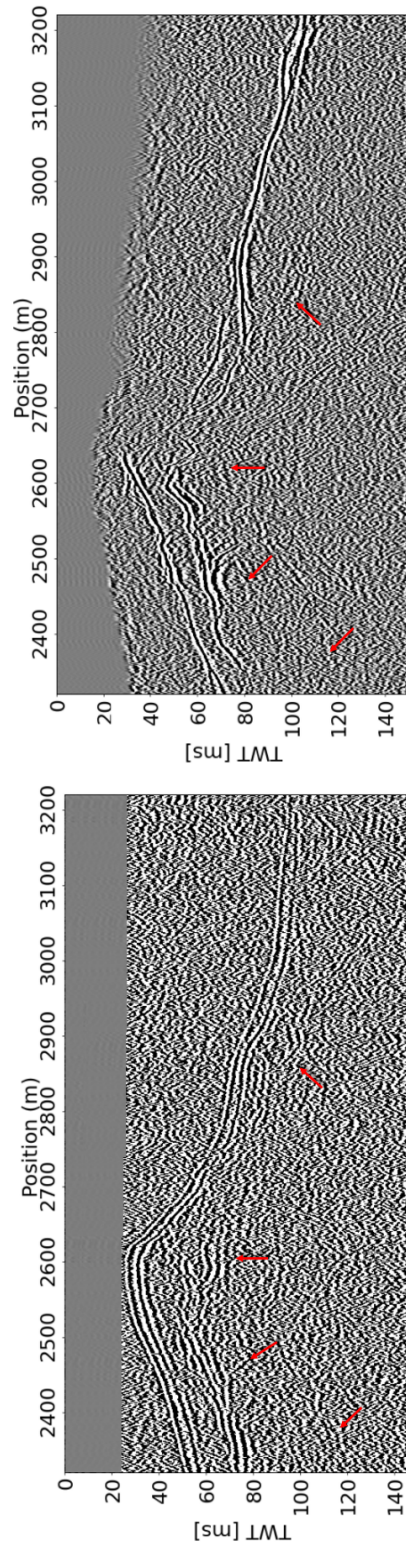
Figure 45: Comparison between (a) Final output image from Streamer. (b) Final output image from DAS. Notice, both images were able to image the structure in the subsurface. The seafloor and basement top can be seen from both images, moreover, some inter-basement reflector, marked by red arrows, can be compared as well from both images.

8   Conclusion

Distributed acoustic sensing (DAS), which is a newly emerging technology that transforms submarine telecommunication cables into densely sampled seismic receivers that are cost effective has been tested in this study, to be used as an alternative method for subsurface imaging in the marine environment. The data has been acquired in the Trondheimsfjord, Norway. We have found that DAS is sensitive to the longitudinal strains, that maximum amplitude from DAS is correspondent to a horizontal incidence angle θ, when wavefields impinge the cable in parallel direction to the cable orientation. The amplitudes starts to decrease as the incidence angle θ increases . Wide azimuth acquisition and an energetic source with a sufficient power should be used, to make up for the amplitude loses due to the DAS directivity. From the frequency difference between the reflected and the direct arrivals in the DAS image, it was clear that the DAS data suffers from a high absorption factor, as a result, it is recommended to use a relatively lower frequencies for deep penetration of the waves inside the Earth. Comparing the DAS image with the image obtained from a streamer data that has been a acquired simultaneously with DAS in the Trondheimsfjord, we have found that both methods have a comparable signal to noise ratio (S/N). We were able to image the subsurface structure by both methods, the main reflectors were successfully imaged as well. DAS data has a lower frequency content than the streamer data and has provided a lower resolution image compared to the streamer, however, it has demonstrated its ability to be used in the marine environment as an alternative technique for subsurface imaging. By little manipulation of the gauge length of the DAS cable and the source energy and frequency we can improve the quality of the image from DAS.

Acknowledgements

References

[1] Thompson M., Arntsen B.,and Amundsen, L., 2007. Experiences with full-azimuth acquisition in ocean bottom seismic. First break, 25(3).

[2] Landrø, M., and Amundsen L., 2018. Introduction to exploration geophysics with recent advances: Bivrost.

[3] Taweesintananon, K., Landrø, M., Brenne, J. K., Haukanes, A. (2021). Distributed acoustic sensing for near-surface imaging using submarine telecommunication cable: A case study in the Trondheimsfjord, Norway. *Geophysics* , 86(5), B303-B320. doi: 10.1190/GEO2020-0834.1

[4] Fang, G., Li, Y. E., Zhao, Y., Martin, E. R. (2020). Urban Near-Surface Seismic Monitoring Using Distributed Acoustic Sensing. Geophysical Research Letters, 47(6), e2019GL086115.

[5] Parker, T., Shatalin, S., Farhadiroushan, M. (2014). Distributed acoustic sensing — A new tool for seismic applications. First Break, 32(2).

[6] Lumens, P. G. E. (2014). Fibre-optic sensing for application in oil and gas wells : P. hD thesis, Eindhoven University of Technology

[7] Lindsey, N. J., Yuan, S., Lellouch, A., Gualtieri, L., Lecocq, T., Biondi, B. (2020). City-scale dark fiber DAS measurements of infrastructure use during the COVID-19 pandemic : Geophysical research letters, 47(16). doi:10.1029/2020GL089931

[8] Ajo-Franklin, J., Lindsey, N., Dou, S., Daley, T. M., Freifeld, B., Martin, E. R., ... Wagner, A. (2015, October). A field test of distributed acoustic sensing for ambient noise recording : 85th Annual International Meeting, SEG, Expanded Abstracts, 2620–2624, doi: 10.1190/segam2015-5926936.1.

[9] Dou, S., Lindsey, N., Wagner, A. M., Daley, T. M., Freifeld, B., Robertson, M., ... Ajo-Franklin, J. B. (2017). Distributed Acoustic Sensing for Seismic Monitoring of The Near Surface: A Trafc-Noise Interferometry Case Study. Scientific REPOrTS — 7: 11620 . doi:10.1038/s41598-017-11986-4

[10] Masoudi A., Newson, T. P. (2016). Contributed Review: Distributed optical fibre dynamic strain sensing. Review of scientific instruments,87(1), 011501, https://doi.org/10.1063/1.4939482

[11] Posey, R., Johnson, G. A., Vohra, S. T. (2000) Rayleigh scattering based distributed sensing system for structural monitoring. In Proc. SPIE (Vol. 4185, p. 41850E). doi: 10.1117/12.2302157

[12] Hartog, A. H., (2017). An introduction to distributed optical fibre sensors. CRC Press.

[13] Waagaard, O. H., Rønnekleiv, E., Haukanes, A., Stabo-Eeg, F., Thingbø, D., Forbord, S., ... Brenne, J. K. (2021). Real-time low noise distributed acoustic sensing in 171 km low loss fiber: Real-time low noise distributed acoustic sensing in 171 km low loss fiber: OSA Continuum, 4(2), 688-701, doi: 10.1364/OSAC.408761

[14] Monrigal, O., de Jong, I., Duarte, H. (2017). An ultra-high-resolution 3D marine seismic system for detailed site investigation Near Surface Geophysics, 15(4), 335-345, doi: 10.3997/1873-0604.2017025.

[15] Dondurur, D. (2018). Acquisition and Processing of Marine Seismic Data, Elsevier.

[16] Peak Seismic Solutions, Ocean bottom seismic. (n.d.), Retrieved March 20, 2018, http://www.peakseismic.com/content/ocean-bottom-seismic.asp

[17] Kowarik, S., Hussels, M. T., Chruscicki, S., Münzenberger, S., Lämmerhirt, A., Pohl, P., Schubert, M. (2020). Fiber Optic Train Monitoring with Distributed Acoustic Sensing: Conventional and Neural Network Data Analysis Sensors,20(2), 450; doi:10.3390/s20020450

[18] Ajo-Franklin, J., Dou, S., Daley, T., Freifeld, B., Robertson, M., Ulrich, C., ... Wagner, A. (2017, September). Timelapse Surface Wave Monitoring of Permafrost Thaw Using Distributed Acoustic Sensing and a Permanent Automated Seismic Source SEG International Exposition the 87th Annual Meeting. doi:10.1190/segam2017-17774027.1

[19] Bakulin, A., Silvestrov, I., Pevzner, R. (2019, March) Surface Seismic with DAS Changes Land Acquisition. The SPE Middle East Oil and Gas Conference 2019, Paper Number: SPE-194950-MS. https://doi.org/10.2118/194950-MS

[20] Silixa, https://silixa.com/resources/what-is-distributed-sensing/

[21] Bertholds, A., Dandliker, R. (1988). Determination of the individual strain-optic coefficients in single-mode optical fibres: Journal of Lightwave Technology, 6(1), 17-20, doi: 10.1109/50.3956

[22] Kuvshinov, B. N. (2016). Interaction of helically wound fibre-optic cables with plane seismic waves: Geophysical Prospecting 64(3), 671-688, doi: 10.1111/1365-2478.12303

[23] Bakku, S. K. (2015). Fracture characterization from seismic measurements in a borehole : Ph.D. thesis, Massachusetts Institute of Technology.

[24] Drijkoningen, G. G. (2003). Lecture notes: Seismic data acquisition – TA3600: Delft University of Technology, Section Applied Geophysics and Petrophysics.

[25] Bakulin, A., Silvestrov, I., Pevzner, R. (2020). Surface seismics with DAS: An emerging alternative to modern point-sensor acquisition : The Leading Edge, 39(11), 808-818, doi: 10.1190/tle39110808.1.

[26] Dondurur, D. (2018). Acquisition and Processing of Marine Seismic Data, Elsevier.

[27] Roberts, D. (1998). Geology of the Fosen Penissula and Trondheimsfjord Region: a synopsis and excursion guide Geological survey of Norway (NGU), Report number 98.119.

[28] Bøe, R., Vigran, J. O., Roberts, D., Mørk, M. B. E. (2005). Possible Mesozoic sediments in fault and brecciation zones in Frøyfjorden, Mid Norway, Norges geologiske undersøkelse 443, 29-35

[29] Rise, L., Bøe, R., Sveian, H., Lyså, A., Olsen, H. A. (2006). The deglaciation history of Trondheimsfjorden and Trondheimsleia, Central Norway Norwegian Journal of Geology, Vol. 86, pp. 419-438., ISSN 029-196X.

[30] Bøe, R., Bjerkli, K. (1989). Mesozoic sedimentary rocks in Edøyfjorden and beitstadfjorgen centeral Norway: implications for structural history of the Møre-Trondelag Fault Zone. Marine Geology 87(2-4), 287-299.

[31] Grønlie, A., Torsvik, T. H. (1989). On the origin and age of hydrothermal thoriumenriched carbonate veins and breccias in the Møre-Trøndelag Fault Zone, Central Norway. Norsk Geologisk Tidsskrift, 69(1), 1-19.

[32] Reite, A. (1994). Weichselian and Holocene geology of Sør-Trøndelag and adjacent parts of Nord-Trøndelag county, Central Norway. Norges geologiske undersøkelse Bulletin 426, 1- 30.

[33] Svjeian, H. (1997). Ice marginal deposits and deglaciation chronology in Nord-Trøndelag and Fosen, Central Norway. Norges geologiske undersøkelse Bulletin 433, 52-53.

[34] Roberts, D., Wolff, F. C. (1981). Tectonostratigraphic development of the Trondheim Region, Norway. Struct. Geol. 3(4), 487-494.

[35] LL'Heureux, J. S., Hansen, L., Longva, O. (2009). Development of the submarine channel in front of the Nidelva River, Trondheimsfjorden, Norway. Marine Geology 260(1-4), 30-44 . doi:10.1016/j.margeo.2009.01.005

[36] Wang, Y., Yuan, H., Liu, X., Bai, Q., Zhang, H., Gao, Y., Jin, B. (2019). A Comprehensive Study of Optical Fiber Acoustic Sensing. IEEE Access, VOLUME 7. doi: 10.1109/ACCESS.2019.2924736

[37] Ma, G. M., Zhou, H. Y., Shi, C., Li, Y. B., Zhang, Q., Li, C. R., Zheng, Q. (2018). Distributed partial discharge detection in a power transformer based on phase-shifted FBG. IEEE Sensors J., vol. 18, no. 7, pp. 2788–2795,

[38] Dong, Y., Zhang, H., Chen, L., Bao, X. (2012). 2 cm spatial-resolution and 2 km range Brillouin optical fiber sensor using a transient differential pulse pair. Appl. Opt., vol. 51, no. 9, pp. 1229–1235, Mar. 2012.

[39] Weng, Y., Ip, E., Pan, Z., Wang, T. (2016). Advanced spatial-division multiplexed measurement systems propositions—From telecommunication to sensing applications: A review. Sensors, vol. 16, no. 9, p. 1387, Sep. 2016.

[40] Langhammer, J., Eriksrud, M., Nakstad, H. (2010). Performance characteristics of 4C fiber optic ocean bottom cables for permanent reservoir monitoring. Conference: SEG Technical Program Expanded Abstracts , DOI:10.1190/1.3513871

[41] Dean, T., Cuny, T., Hartog, A. H. (2017). The effect of gauge length on axially incident P-waves measured using fibre optic distributed vibration sensing Geophysical Prospecting 65(1), 184-193. doi: 10.1111/1365-2478.12419

[42] Wolff, F. C. (1976). Geologisk kart over Norge, berggrunnskart Trondheim 1.250 000. Geological Survey of Norway (NGU).

[43] Bakku, S. K., Wills, P., Fehler, M., Mestayer, J., Mateeva, A., Lopez, J. (2014, October) Vertical Seismic Profiling Using Distributed Acoustic Sensing in a Hydrofrac Treatment Well. SEG Technical Program Expanded Abstracts : 5024-5028. https://doi.org/10.1190/segam2014-1559.1